MDPI

Article

Influence of Ultrahigh Dilution Treatment of the Charge on the Growth and Spectroscopic Properties of Nd:MgMoO$_4$ Potential Laser Crystal

Kirill A. Subbotin [1,2], Yana S. Didenko [1,2,*], Anatolii I. Titov [1], Denis A. Lis [1], Sergei K. Pavlov [1,2], Pavel A. Volkov [3], Kristina I. Runina [2], Valerii V. Voronov [1], Elena V. Chernova [1], Olga N. Lis [1], Kristina V. Kuleshova [1,2] and Yulia I. Zimina [1,2]

[1] Prokhorov General Physics Institute of the Russian Academy of Sciences, Vavilova Str. 38, Moscow 119991, Russia; soubbot@lsk.gpi.ru (K.A.S.); anatoly.titov.4@gmail.com (A.I.T.); lisdenis@mail.ru (D.A.L.); sergey.pavlov97@mail.ru (S.K.P.); voronov@lst.gpi.ru (V.V.V.); e-chernova@yandex.ru (E.V.C.); ozaytceva@mail.ru (O.N.L.); kristinka-0601@mail.ru (K.V.K.); yulia_zimina@inbox.ru (Y.I.Z.)

[2] Department of Chemistry and Technology of Crystals, Mendeleev University of Chemical Technology, Moscow 125047, Russia; runinakristina@mail.ru

[3] NRC "Kurchatov Institute"—IREA Shared Knowledge Center, Bogorodskii Val Str. 3, Moscow 107076, Russia; volkov.pavel.msu@yandex.ru

* Correspondence: ia.didenko@yandex.ru

Abstract: The influence of the charge treatment by ultrahigh dilution (UHD) technology on oxide single crystals grown by the Czochralski technique was studied for monoclinic MgMoO$_4$ crystals doped by 1 at. % of Nd^{3+} ions. The series of 10 Nd:MgMoO$_4$ crystals was grown from the charges that were subjected to UHD treatment, as well as from the charges treated with two types of control or with no special treatment at all. The grown crystals were studied by X-ray powder diffraction analysis, inductively coupled plasma atomic emission spectroscopy, mass-spectrometry, optical absorption, emission spectroscopy and luminescence kinetic analysis. We found that: (i) wetting of MgO + MoO$_3$ mixture by a water-ethanol solution before calcining leads to some enrichment of the mixture with MoO$_3$, whereas the wetting of the charge after the calcining leads to some enrichment of it with MgO; (ii) congruent melting composition of MgMoO$_4$ crystal is in the field of some MoO$_3$ excess; (iii) the solid-phase solubility of the excess MoO$_3$ in MgMoO$_4$ probably does not depend on temperature, whereas the solid-phase solubility of the excess MgO in MgMoO$_4$ crystal depends on temperature. We suggest that the corresponding solidus line passes through the range of retrograde solubility; (iv) the crystals grown within this range are characterized by the enhanced Nd^{3+} segregation coefficient between the crystal and the melt (approximately 0.006 versus 0.004); (v) unit cell parameters of MgMoO$_4$ crystal with the excess of MoO$_3$ are larger than those of the crystal of the stoichiometric composition and of the crystal with the excess of MgO; (vi) the shapes of the optical absorption and luminescence spectra of Nd:MgMoO$_4$ crystal do not depend on the charge treatment; (vii) luminescence decay kinetics are single-exponential for all the studied crystals, the luminescence decay time being different for the crystals grown from the charges that underwent different types of treatment; (viii) the luminescence intensity of Nd:MgMoO$_4$ crystal grown from the charge that underwent UHD treatment before calcining (solid-phase synthesis) is reduced by an order of magnitude in comparison with the other studied crystals.

Keywords: molybdates; neodymium ion; magnesium molybdate; crystal growth; ultrahigh dilution technology; luminescence; crystal structure

1. Introduction

Ultrahigh dilution (UHD) technology has been used in the pharmaceutical industry for decades. UHD solutions are obtained by the sequential technological processing of

various substances, for example, antibodies. These technologically-processed solutions can then acquire novel long-lasting biological and physico-chemical properties compared both to the non-treated substances and to the solvents [1–3]. These effects can depend on the initial substance and on a targeted system [4]. In particular, it was previously shown that the properties of water and water-based solutions processed with UHD technology are changed [5–8]. Due to their acquired physical and chemical features, these solutions can influence not only biological systems [9–12] but even inorganic functional materials [13]. For example, UHD technology has been shown to modify the functional characteristics and porosity of the ceramic superconductor [14] and of the hot-pressed piezoelectric material [15]. Therefore, it is quite possible that UHD solutions can also influence single-crystalline structures. However, we failed to find in the available literature any information about the attempts to apply UHD technology to such kinds of objects.

There is no general theory about what interactions that occurr during UHD treatment cause these experimentally observable effects. However, a few possible explanations do exist. In fact, mechanical impact on the solution can cause new properties through a few possible mechanisms. Some authors [3,16] affirm that spontaneous formation of nanoassociates takes place. Others show that nanobubbles can form in the solution due to the effects of cavitation [17] and/or compression [18] of pre-existing microbubbles. These nanobubbles might be captured by a crystal and sufficiently influence the structures of highly organized crystals. Thirdly, it is possible that even highly diluted samples of some substances can still carry meaningful amounts of those substances due to the effects of flotation, where molecules are bound to the aforementioned nanobubbles [16,19]. These effects can occur in many physical systems. They can have a number of profound effects when the precise and exact properties of systems are of the utmost importance. For example, it is known that nanobubbles affect cement hardening [20,21] and petroleum properties [22–24].

The main aim of this research was to test the influence of UHD treatment of the initial charges on the growth of single crystals from these charges and onto the properties of the obtained crystals. We have chosen a Nd-doped $MgMoO_4$ single crystal as the model object due to the following reasons:

1. $MgMoO_4$ crystal melts congruently, therefore, it can be easily grown by the simple, fast and mature Czochralski technique. The first successful attempts to grow $MgMoO_4$ single crystals by this technique were reported in 1963 [25] and 1966 [26]. Later, this technique was successfully used for the growth of both undoped $MgMoO_4$ crystals [27–29] and of the crystals doped with Gd^{3+}, Fe^{2+} [30], Yb^{3+} [27] and Tm^{3+} [31] ions. Moreover, due to the rather low melting point of 1320 °C [32], the growth process can be performed from Pt crucible in air. Thus, series of the crystals can easily be grown reproducibly within a rather short period of time and without uncertainties in the growth atmosphere from sample to sample within the series.

2. $MgMoO_4$ crystal has two well-expressed cleavage planes along the (9 11 0) and (11 9 0) crystallographic planes [27,33]. The cracks appearing in the crystal along these planes, allowing for easy determination of the sample orientations with respect to the crystallographic axes in order to perform the polarized spectroscopic studies of the crystals.

3. No rare-earth ions are involved in the composition of the $MgMoO_4$ host. Therefore, we can choose quite easily the batches of the starting materials, MgO and MoO_3, containing negligibly low concentrations of the accidental impurities of rare-earth ions (see below). Otherwise, if we would choose a host containing rare-earth components in its composition (e.g., YAG, YVO_4, KGW, YLF, etc.), it will be a rather difficult problem to find the commercially available batches of chemicals (Y_2O_3, YF_3, Gd_2O_3, etc.) for a reasonable price with low enough concentrations of the spectroscopically active rare-earths accidental impurities (Nd, Er, Pr, Ce, etc.) because the chemical properties of all rare-earths are very close. Therefore, their deep purification from each other is complicated. On the other hand, the presence of such accidental impurities may distort the results of the spectroscopic measurements.

4. Nd-doped crystals possess a very bright and well-studied luminescence even at rather low concentrations of the dopant, with an easily measurable lifetime at room temperature. Therefore, Nd^{3+} ion is a very good spectroscopic probe.

5. The optical, spectroscopic [27,34–39] and some other [40–42] properties of undoped $MgMoO_4$ have been extensively studied at this moment. Some data are also available in the literature on the spectroscopic properties of $MgMoO_4$ crystals and powders or nanoparticles doped with Yb^{3+} [27,43], Cr^{3+} [40,44], Tm^{3+} [31], Eu^{3+} [45,46], Eu^{3+}, Dy^{3+} [47] and Eu^{3+},Bi^{3+} [48] ions/ion pairs. The results of these studies have shown that $MgMoO_4$ is interesting for applications in scintillators [27,34], phosphors [37,46,49] and laser hosts [31,40]. Along with that, the $MgMoO_4$ powder is widely used as a catalyst for the dehydrogenation of saturated hydrocarbons [50,51]. Meanwhile, we have failed to find any information about studies of $Nd:MgMoO_4$ single crystals in the available literature. Therefore, our present research should result in the obtaining of novel results, regardless of whether the influence of charges' UHD-treatment on the crystal growth properties will be found or not.

The structure of $MgMoO_4$ (Figure 1) is monoclinic with the $C2/m$ space group and the $2/m$ point group. The unit-cell parameters are: $a = 10.273(3)$ Å, $b = 9.288(3)$ Å, $c = 7.025(2)$ Å and $\beta = 106.96°$ [52]. The structure is layered: the layers of two non-equivalent kinds of MgO_6 octahedra formed around Mg1 (Wyckoff: 4g) and Mg2 (Wyckoff: 4i) sites are separated by the layers of two non-equivalent kinds of MoO_4 tetrahedra. The neighbouring MgO_6 octahedra are connected by the shared edges. According to structure refinement and electronic paramagnetic resonance (EPR) studies, the dopant RE^{3+} ions tend to replace the host-forming cations Mg^{2+} in the sub-lattice Mg1 [30,48]. This is because of the stronger distortion of the $Mg1O_6$ octahedra and longer Mg1–O distances tolerating the difference in the ionic radii between Mg^{2+} and considerably larger rare-earth ions, as compared to the almost ideal $Mg2O_6$ octahedra with shorter metal–oxygen interatomic distances.
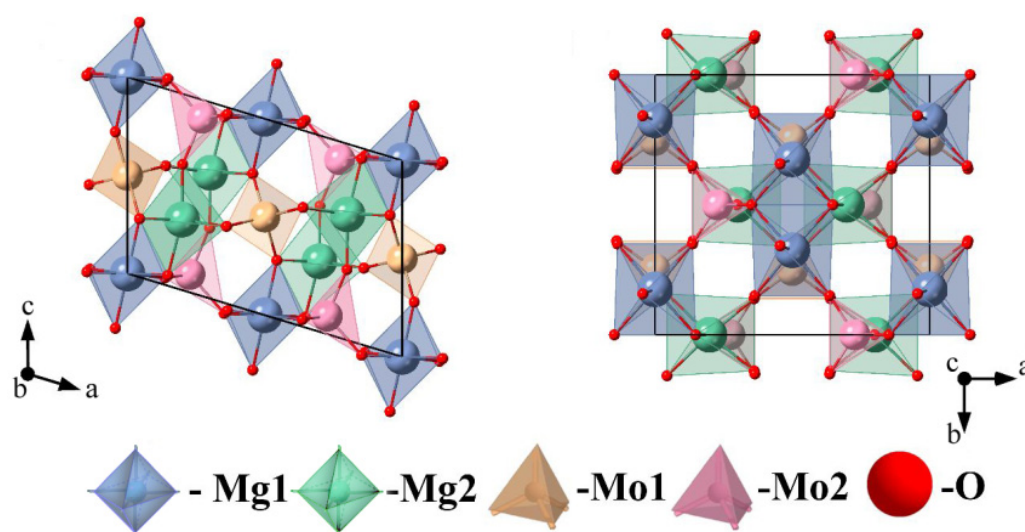

Figure 1. Structure of $MgMoO_4$ in two crystallographic projections (black lines, unit-cell). Reprinted with permission from Ref. [35].

2. Materials and Methods

2.1. Starting Materials

For the charge synthesis we have used the following highly pure starting materials: MgO (Sigma-Aldrich, Burlington, MA, USA), MoO_3 (Lankhit Ltd., Moscow, Russia) and Nd_2O_3 (Nd-E, OST 48-200-81 post-box M 5998, former USSR). Firstly, we have measured the actual accidental impurity compositions of MgO and MoO_3 by inductively-coupled plasma mass-spectrometry (ICP MS) analysis. The measurements were performed on a NexION 300D inductively coupled plasma mass spectrometer (PerkinElmer Inc., Waltham, MA, USA) using the kinetic energy discrimination mode. The TotalQuant method [53] was

used for the determination of the concentrations of 65 chemical elements. The standard solutions (PerkinElmer Inc., Shelton, CT, USA) were used for calibration. The results of the measurements are presented in Figure 2. The data for Mg, Mo and the elements with concentrations below 1×10^{-8} wt.% (0.1 ppb) are omitted in both diagrams. Along with that, Ti and Cd concentrations in MoO_3 cannot be measured by ICP MS analysis because of the interference of the signals of these ions with those of Mo^{2+} and MoO^+ ions, respectively.
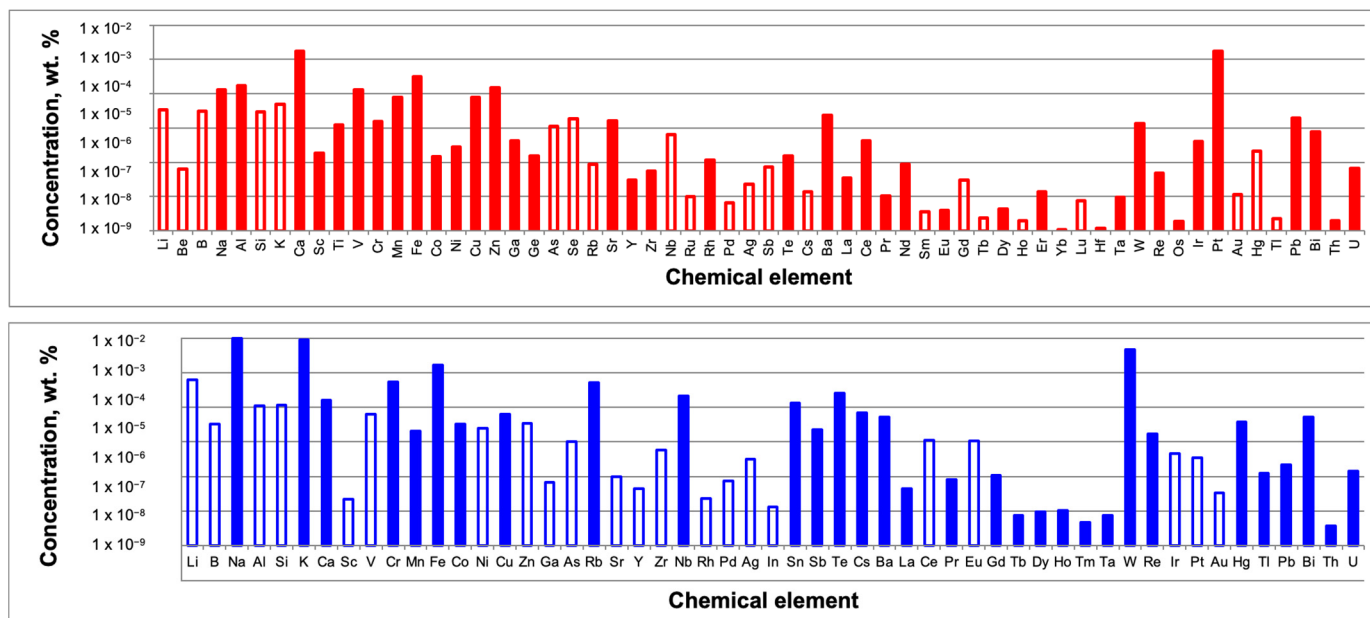

Figure 2. Accidental impurity compositions of MgO (**upper**) and MoO_3 (**lower**) starting materials used in the research. The filled bars indicate the concentrations of the detected elements, while the empty bars indicate the detection limits for the elements with the concentrations below these limits.

Figure 2 shows that among the optically active rare-earth accidental impurities, the highest concentration was 4×10^{-6} wt.% (for cerium ion in MgO). We believe that such concentrations cannot substantially change the spectroscopic properties of the Nd^{3+} dopant in the grown Nd:MgMoO$_4$ crystals. Along with that, some 3D-impurities were revealed in the chemicals. For example, iron had a concentration of 1.6×10^{-3} wt.% which, in principle, may influence the spectroscopic results.

For Nd_2O_3 starting material, the measurement of the actual impurity composition was not performed. The purity declared by the supplier was "4N".

2.2. Charges Preparation and UHD Treatment

To prepare the charges for crystal growth, the starting materials were dried before weighing. For drying, MoO_3 and Nd_2O_3 were put into new corundum crucibles with covers. The drying was performed in an EKPS-10/1250 SPU 4107 muffle furnace (Russia) at 700 °C for 5 h. The drying of MgO was performed at 1250 °C for 5 h, and the chemical was put into a platinum cup with a cover.

After drying, the required amounts of MgO and MoO_3 were weighed on an Adventurer AX523 electronic analytical balance (OHAUS, Parsippany, NJ, USA) with a precision of 0.001 g to obtain the basic batch B_0 of the undoped MgO + MoO_3 mixture with a total weight of 350 g (Figure 3). This batch was then put into a new polypropylene container and thoroughly blended with the help of a Multi RS-60 mixer-rotator (BioSan, Latvia). This batch was then used for synthesis of all 10 Nd:MgMoO$_4$ crystalline samples.
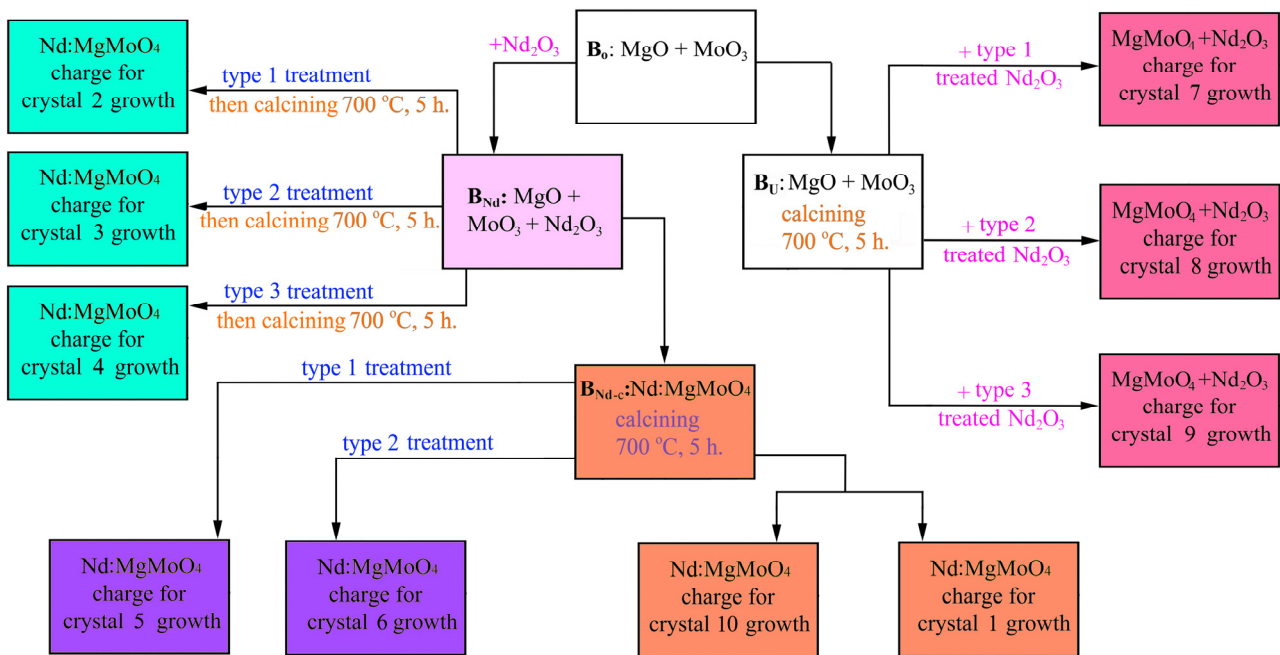
Figure 3. Scheme depicting the methodological procedures of the preparation of charges.

In particular, a part of the B_o basic batch containing 245 g (enough for the growth of 7 crystals) denoted as the batch B_{Nd} was then doped by Nd^{3+} (1 at. % in respect to Mg) by addition of the appropriate amount of Nd_2O_3. The obtained mixture was thoroughly blended again. The rest of the B_o basic batch containing 105 g (enough for 3 crystals), denoted as the batch B_u, temporarily remained undoped (Figure 3). Then, a part of B_{Nd} batch, denoted as B_{Nd-c} (totally 140 g, enough for 4 crystals) was calcined at 700 °C for 5 h simultaneously with the B_u batch (in the same furnace but in different containers) to perform a solid phase synthesis of the compound.

Next, part of the calcined B_{Nd-c} batch was divided into two equal parts, which were used for the growth of crystals 1 and 10 without any additional procedures (hereafter, charges 1 and 10). The rest of B_{Nd-c} batch was also divided into two equal parts, which have undergone two different types of special treatment (see below). After the treatments, they were used for growth of the crystals 5 and 6 (charges 5 and 6, respectively). See Figure 3.

The rest of the B_{Nd} batch (totally 105 g) was divided into three equal parts, which have undergone three different types of special treatment. After the treatments, they were simultaneously (but in separate new corundum crucibles) calcined at 700 °C for 5 h to perform a solid-phase synthesis of the compound. The obtained three batches (charges 2, 3 and 4) were used for the growth of the crystals 2, 3 and 4, respectively.

Finally, the B_u batch containing the calcined undoped charge was divided into three equal parts. Each of these parts was then doped with a corresponding portion of Nd_2O_3. Each portion of Nd_2O_3 was preliminarily subjected to a different type of special treatment. The obtained batches of the charge (charges 7, 8 and 9) were then used for growth of Nd:MgMoO$_4$ crystals 7, 8 and 9. The procedures for preparation of the charges for growth of the studied crystals are summarized in Figure 3.

Special treatments of the charges were performed by OOO "NPF "MATERIA MEDICA HOLDING." Three different types of special treatment were used. The principles of these treatments are similar to the ones described in detail in [54]. It is briefly summarized below.

Treatment type 1 is UHD treatment. It included mixing the charge (65 g) with 30 g of an ultra-highly diluted water-ethanol (36.7%) solution of the same charge. In the case of charge 7, only the dopant was treated by UHD (see Figure 3). In this case, 2 g of Nd_2O_3 powder were mixed with 1.3 g of ultrahigh water-ethanol dilution of Nd_2O_3. After mixing,

the obtained suspensions were stirred with a glass rod until homogeneity was reached and then dried at 35 °C for at least 6 h until the liquid completely evaporated.

Treatment type 2 included mixing the charge (or Nd_2O_3, in the case of charge 8) with the technologically processed (see below) water-ethanol solution, instead of the ultrahigh water-ethanol dilution of the charge (Nd_2O_3) as was conducted during type 1 of special treatment. Treatment type 3 included mixing of the charge (or Nd_2O_3, in the case of charge 9) with a simple (non-processed) water-ethanol solution. All the following procedures (stirring, drying) were the same for all three types of treatment. The treatment types 2 and 3 are control treatments. They were aimed at distinguishing the impact of the UHD treatment and interaction of water-ethanol solution itself with the charges or with their components.

The preparation of UHD of the charge (or dopant) was performed according to the following procedure. Since the charge-forming oxides (MgO, MoO_3, Nd_2O_3) are insoluble in a water-ethanol solution, the first three steps of sequential decrease in their concentrations (centesimal dilutions) were performed by grinding 1 g of the powders in an agate mortar with SuperTab 30 GR α-lactose monohydrate (α-$C_{12}H_{22}O_{11} \cdot H_2O$) powder (DFE Pharma, Goch, Germany). After such, three centesimal dilutions were performed, and the resulting solid mixture was added to the solvent (an ethanol-water solution) at a ratio of 1:100 by weight and underwent an intensive vibration treatment to produce the fourth centesimal dilution. The subsequent 46 centesimal dilutions were performed using the same procedure. The theoretical concentration reduction of the initial precursor powder mixture was at least 1×10^{24} times.

For treatment type 2, the technological processing of the water-ethanol solution of α-lactose monohydrate (without charges or Nd_2O_3, in contrast to type 1 of UHD treatment) was its 50th sequential centesimal dilutions in a water-ethanol solution.

The preparation of solutions and wetting of powders was performed at room temperature in a laminar flow cabinet under clean conditions to prevent environmental contamination.

The charges 1 and 7–10, prepared from B_U and B_{Nd-c} batches (without a treatment of the host components), were slightly aggregated after calcining. After grinding in an agate mortar, these charges started to appear as loose grey-coloured powders with a minor amount of small yellowish clumps. The charges 5 and 6 made from B_{Nd-c} batch and treated after calcining contained quite solid pale bluish-grey aggregates with sizes of up to several millimeters. The charges 2–4 made from B_{Nd} batch and UHD-treated before calcining contained similar aggregates, but their colour was yellowish. We assume that these differences reflect some changes in the compositions of charges.

3. Results and Discussion

3.1. Crystal Growth, the Actual Crystals Compositions and XRD Studies

The crystals were grown by the Czochralski technique in a "Kristall-2" growth machine (USSR) with RF-heating from Pt/Rh crucible (30 mm in diameter and in height) in air ambient. Prior to the start of the growth process of each crystal, the hot crucible was filled by a charge with pre-melting. This step was performed without the upper part of thermal shields.

Pre-melting behaviour of the charges appeared to be different depending on the procedure for charge preparation; all the charges, except 5 and 6, were melted easily and completely without any problems at reasonable levels of RF-heater power.

Another situation was observed during the pre-melting of the charges 5 and 6 (the only charges calcined before the UHD treatment) (see Figure 3): after easy melting of the charges, a refractory crust was formed at the surfaces of the melts. This suggests some underheating of the melt or precipitation of a second solid phase with comparatively low density from the melt. On the other hand, under this crust, we observed the intensive melt flows through the holes in the crust. Moreover, in case of charge 6 we observed pronounced evaporation from the melt surface, meaning that the melts under the crust were considerably overheated. However, the attempts to submerge the crust by pushing it

down into the melt using Pt wire have resulted in fast crystallization of a part of the melt at this wire (in case of the charge 5). Some increase of RF-heating power (within its reasonable values) resulted only in partial melting of this crust.

After pre-melting and filling the crucible with a charge, it was cooled down to room temperature. Single-crystalline seed cut from undoped $MgMoO_4$ was mounted at the upped stock of the growth machine, and the upper set of thermal shields were installed above the crucible with a frozen melt. The construction of this shield set contains an additional active resistive heater with the temperature control by thermocouple. It allows for the smoothening of the thermal gradients inside the hot growth zone, and for the organizing of the slow (8 °C/h) cooling of the grown crystal to room temperature after finishing the growth process and switching off the main RF-heater.

Before seeding, all the pre-molten charges were completely melted, obtaining a free, mirror-smooth melt surface. We succeeded to achieve such a surface even in the cases of melts 5 and 6 because the additional active resistive heater in the upper part of the thermal shields helped the main RF-heater to heat the melts more uniformly. Only after achieving the mirror-smooth melt surface was a seeding conducted.

Rather often, at various stages of the growth processes, numerous dark, suspension-like formations appeared at the melt surfaces. These formations are most certainly conglomerates of second solid phase precipitates. From this point on, these formations are designated as "mush." This "mush" was actively captured by the lateral surfaces of the crystals with the formation of the inclusion-containing areas (Figures 4 and 5). This process destabilized the crystals diameters (Figure 4). Bulk parts of the crystals were almost free from such areas. Therefore, we can conclude that the "mush" fragments were floating near the melt surface rather than distributed uniformly in the bulk of the melt. The "mush"-capturing areas microscopically looked as multiple faceted particles with an amber colour and sizes of up to 0.1 mm dispersed in the main transparent light-yellow crystallite phase (Figure 5).
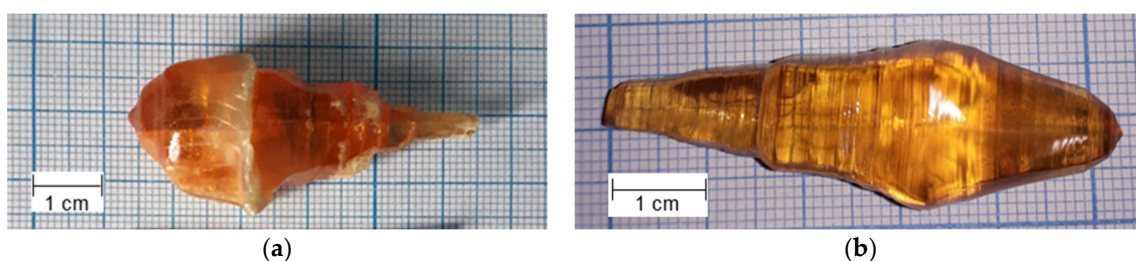

(a)   (b)

Figure 4. Photos of crystal 1 with numerous "mush" captures (**a**) and of crystal 3 with no "mush" captures [31] (**b**).
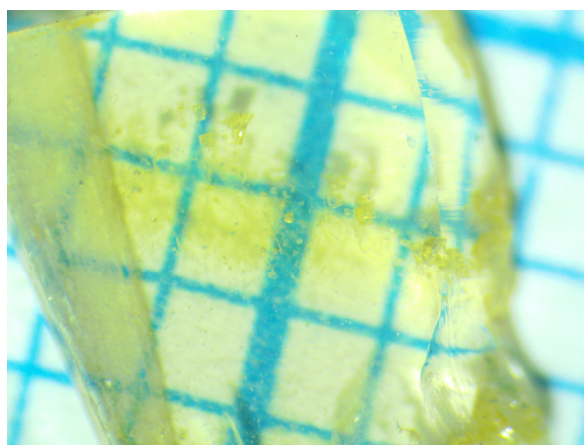

Figure 5. Optical microscope image of part of the crystal 1 containing "mush" capture.

We believe that the above-noted refractory crust, formed at the surfaces of the melts 5 and 6 during pre-melting of the charges, has the same nature as the "mush." We attempted to analyze the phase compositions of these inclusions by X-ray powder diffraction (XRD) analysis using a Bruker D8 Discover A25 DaVinci X-ray diffractometer over a 2θ range of 10–70°, with a step size of 0.02° and step exposure time of 1.5 s. In fact, some of the XRD pattern appeared to contain the reflexes that are barely recognizable as originating from the main $MgMoO_4$ crystalline phase (JCPDS file 21-0961 Figure 6, yellow arrows) or cannot be identified as the main phase at all (Figure 6, red arrows).
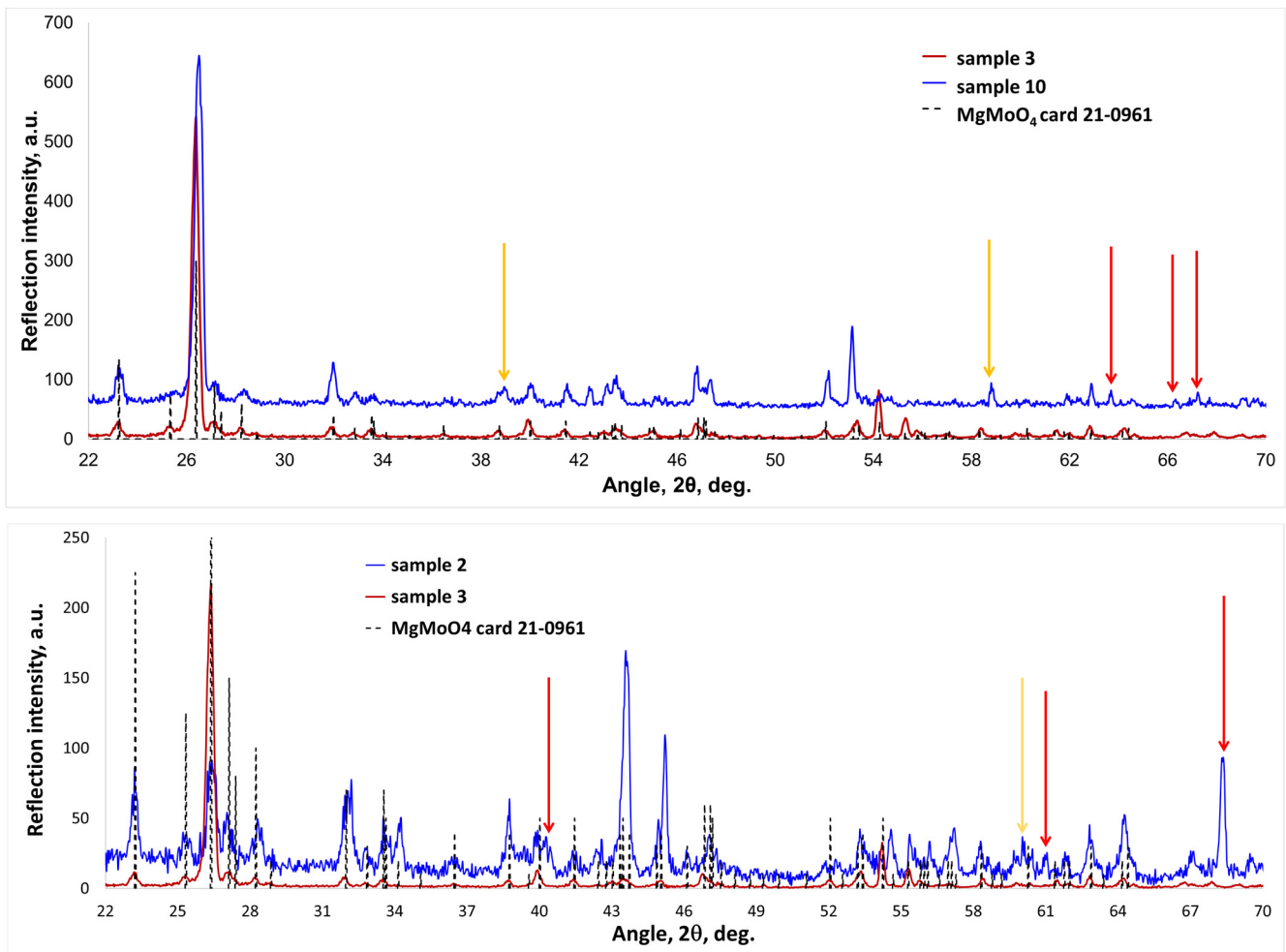

Figure 6. Examples of the XRD patterns of the samples 10 (**upper**) and 2 (**lower**) containing the second phases, in comparison to the one for the sample 3 free from the second phases. Yellow arrows are, presumably, the reflexes of second crystalline phases; red arrows are certainly the reflexes of second crystalline phases.

The majority of the observed lateral reflexes are rather weak in the majority of the samples and we failed to ascribe them unequivocally to any particular second phase. Moreover, the sets of the unidentified reflexes differ from sample to sample.

We also measured the actual composition of the obtained crystals. The measurements were performed by inductively coupled plasma mass spectrometry (ICP-MS) using an Elan DRC-e mass-spectrometer (Perkin Elmer, Shelton, CT, USA). For the analysis, the samples ground into powders beforehand were dissolved in an extra-pure phosphoric acid (Suprapur, Merck, Darmstadt, Germany) at temperatures of up to 400 °C.

A set of 5 samples were taken from different parts of each boule for analysis, thus, a total of 50 samples were analyzed (the results are presented in Table 1 and discussed

below). Along with that, an additional set of samples was taken from the areas of the "mush" captured at the lateral surface of crystal 6. The resulting "total" concentration of Mg^{2+} ions in this additional set appeared to be 1.13 ± 0.09 f.u., whereas the "total" content of Mo^{6+} ions appeared to be 0.96 ± 0.03 f.u. (Table 1, the last separate row '6-mush'). The term "total" means that the ICP-MS method cannot measure separately the compositions of different crystalline (or vitreous) phases if they are jointly present in the probe. This method measures only the total amount of each chemical element in the dissolved probe, independently to the type of microparticle, from which the atom has come into the probe solution.

Table 1. Cation concentrations in crystals, measured by ICP-MS.

Sample #	Mg Concentration, f.u.	Mo Concentration, f.u.	Mg/Mo Molar Ratio
1	0.993 ± 0.008	1.002 ± 0.003	0.984 ± 0.004
2	0.979 ± 0.003	1.005 ± 0.001	0.974 ± 0.004
3	0.982 ± 0.002	1.005 ± 0.001	0.977 ± 0.003
4	0.981 ± 0.002	1.0055 ± 0.0004	0.976 ± 0.002
5	0.980 ± 0.003	1.005 ± 0.001	0.975 ± 0.004
6	0.979 ± 0.007	1.005 ± 0.001	0.974 ± 0.009
7	0.982 ± 0.001	1.0054 ± 0.0003	0.977 ± 0.002
8	0.983 ± 0.002	1.005 ± 0.001	0.979 ± 0.003
9	0.984 ± 0.002	1.005 ± 0.001	0.979 ± 0.002
10	0.986 ± 0.004	1.004 ± 0.001	0.982 ± 0.005
6-"mush"	1.13 ± 0.09	0.96 ± 0.03	1.2 ± 0.1

The typical concentrations of Mg^{2+} ions in the single-phase $MgMoO_4$ crystalline samples are ~0.98 f.u., whereas the ones for Mo^{6+} ions are ~1.005 f.u. (see Table 1). Therefore, the "mush" capturing areas of crystal 6 contain ~15% of Mg^{2+} excess and ~5% of Mo^{6+} deficiency as compared to the inclusion-free areas of the crystals (including crystal 6). From this result we can conclude that "mush"-forming areas are the mixtures of the main $MgMoO_4$ crystalline phase and the inclusions of MgO or of a so far unknown magnesium molybdate phase with the $MgO:MoO_3$ molar ratio exceeding 1:1. Such phases are not mentioned in the MgO-MoO_3 phase diagram (Figure 7).

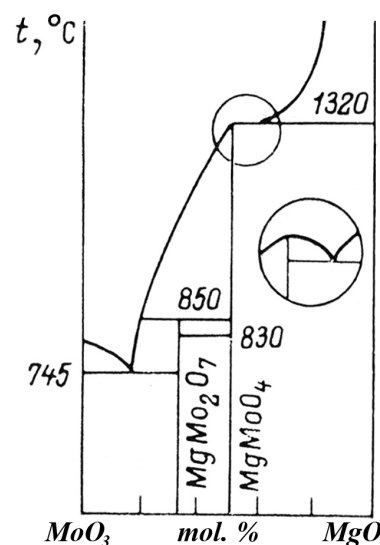**Figure 7.** Phase diagram of MgO-MoO_3 system. Reprinted with permission from Ref. [54].

There is an additional indirect confirmation of this conclusion: the density of MgO at room temperature is 3.58 g/cm^3 [55], less than the density of MgMoO$_4$ (3.87 g/cm^3 [56]). Unfortunately, the data on the similar values at 1322 °C, as well as on the density of MgMoO$_4$ melt, are unavailable. However, if the ratios between the densities at high temperatures are similar to those at room temperature, then the solid MgO (or another Mg-enriched) inclusions should float near the MgMoO$_4$ melt surface. This exact situation was observed.

The "mush" formation behaviour of the melts during crystal growth strongly depends on the procedure of the charges' preparation. In the case of charges 5 and 6 (treated after the calcining), the "mush" started to form immediately after a crystal neck formation under the influence of a very slight reduction of the RF heating power, performed for starting the increase of a crystal diameter. However, after some period of growth, the "mush" disappeared without any evident additional external impact (captured by the crystal with no formation of new portions of the "mush" inside a melt), and the final stages of the crystals were grown from clear melt surfaces.

The opposite situation was observed for the crystals grown from the charges, the main components of which did not undergo any treatment (charges 7, 9 and 10), as well as for the crystal grown from charge 4, which was only mixed with standard water-alcohol solution (control). In these cases, the starting and quite substantial parts of the crystals were grown from clear melt surfaces. The "mush" started to form only after some time during the nominal growth process. However, once it appeared, the "mush" did not go away until the end of the growth.

Finally, the charges that were treated by UHD before calcining (charges 2 and 3) demonstrated no "mush" formation during the growth process.

There were only two exceptions to this regularity:

1. charge 1, which behaves like the UHD treated charges after calcining (5 and 6), although this charge was not treated at all;

2. charge 8, behaving like the charges whose main host components were treated before calcining (2 and 3), although the host components of this charge were not treated at all (only the dopant was treated);

As seen from Table 1, the actual molybdenum concentration is almost stable all over the crystals, and it is in slight excess over the stoichiometry. On the contrary, magnesium is in a deficiency in all of the studied crystals, but the extent of this deficiency varies from sample to sample within the essential range. The highest Mg^{2+} concentrations (the smallest deficiencies) are in the crystals 1 and 10, which were grown from the stoichiometric charges prepared without any treatment. All the rest of the crystals that were treated have larger Mg^{2+} deficiency in their compositions.

As seen from the MgO-MoO$_3$ phase diagram (Figure 7), MgMoO$_4$ melts congruently at a temperature slightly exceeding 1330 °C. The precise melting point of MgMoO$_4$ crystal doped with a very low amount of Tm^{3+} ions was determined by DTA to be 1322 °C [32]. However, the available phase diagram does not contain any information either about the precise congruently melting composition (CMC) of magnesium molybdate or about the MgMoO$_4$ homogeneity field in the crystalline state. Meanwhile, based on the measured compositions of crystals and on the revealed "mush" behaviour of the melts during crystal growth, we can make some assumptions on these issues while keeping the following facts in mind:

(i) The Czochralski crystal growth process is not a phase equilibrium.

(ii) 1 at. % of Nd^{3+} in the melts may have some influence on the situation (on the contrary, the actual Nd^{3+} concentrations in the crystals are negligible from the point of view of the possibility to change anything in phase diagrams, see below);

(iii) a single-crystalline MgMoO$_4$ seed touching the melt surface may also have some influence on the situation.

The probable assumptions are as follows (the corresponding supposed view of the vicinity of the MgMoO$_4$ stoichiometry point at the MgO-MoO$_3$ phase diagram is presented in the upper panel of Figure 8):
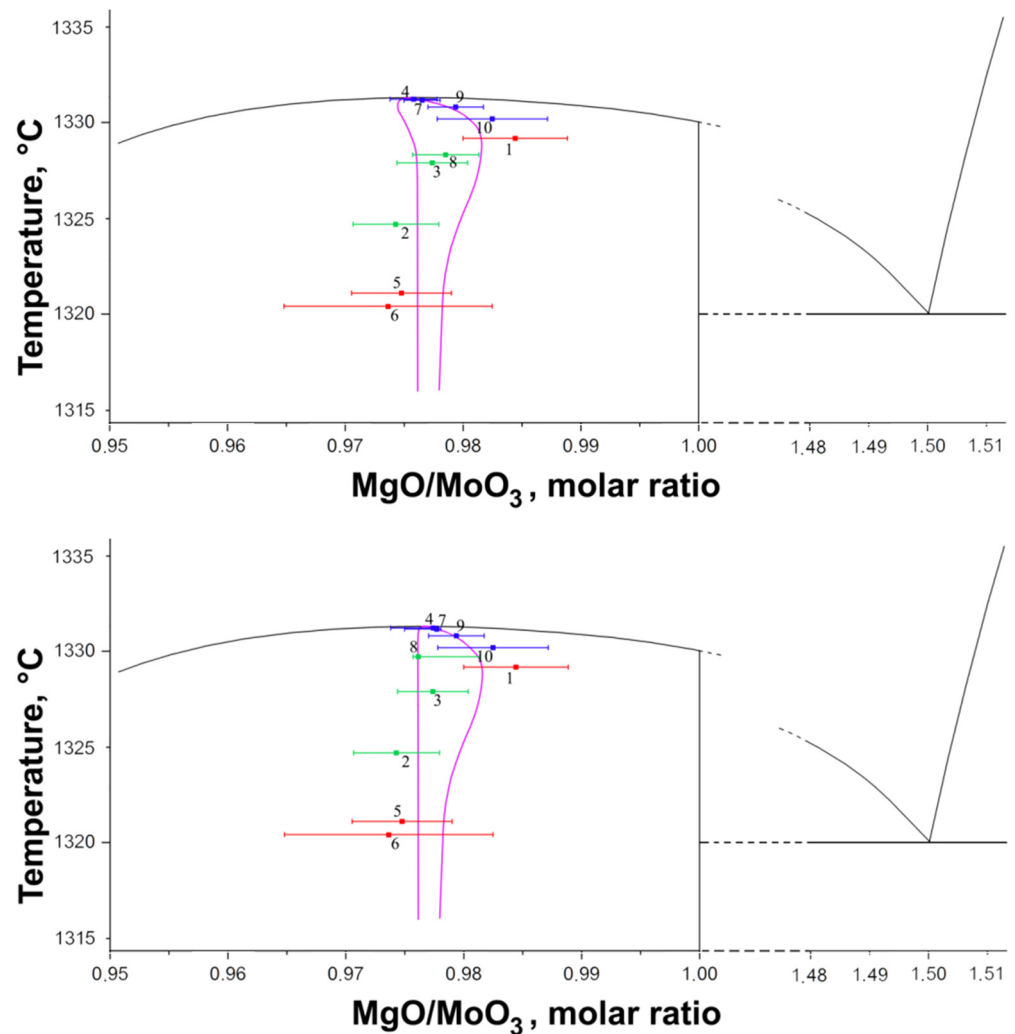

Figure 8. Supposed view of the vicinity of the MgMoO$_4$ stoichiometry point in the MgO-MoO$_3$ phase diagram (two versions). Violet line is the supposed tentative shape of the boundaries of MgMoO$_4$ homogeneity field. Explanation of the experimental points colors is in the main text.

1. We assume crystals 4, 7, 9 and 10 (blue points in the Figure 8) with the actual Mg/Mo molar ratios equal to or exceeding 0.976 were grown from the melts enriched by MgO with respect to the CMC. On the other hand, the charges of these crystals have undergone very slight treatment (charge 4 was only wetted by simple, non-treated water-alcohol solution without any dilutions, whereas for charges 7 and 9, only the dopant was treated, see Figure 3) or had no treatment at all. Thus, it is reasonable to assume that the initial compositions of the melts 4, 7, 9 and 10 are the closest ones to MgMoO$_4$ stoichiometry. Therefore, the CMC for MgMoO$_4$ crystal is in the range of slight MoO$_3$ excess and MgO deficiency in respect to the stoichiometric molar ratio 1:1. In this case, the melt compositions 4, 7, 9 and 10 should gradually shift from their initial values towards deeper enrichment in MgO during the crystallization process, especially taking into account that slow MoO$_3$ evaporation from the melt occurred both during the growth process and during the pre-melting of the charges in the crucible. Due to this shift, the melts should reach the vicinity of the MgMoO$_4$ + MgO eutectic point after some period of time, taking into account that this eutectic point is not very far from the MgMoO$_4$ stoichiometry point (see Figure 8).

This should result in the simultaneous crystallization of $MgMoO_4$ and MgO phases. This situation was probably observed in reality as the "mush" formation.

The actual composition of crystal 1 has larger MgO concentrations than crystals 4, 7, 9 and even 10 (see Table 1). Similarly to sample 10, its initial charge corresponded to $MgMoO_4$ stoichiometry without any treatment. However, the melt of sample 1 was rather strongly overheated during pre-melting. It could lead to substantial MoO_3 evaporation. Thus, we assume that melt 1 probably had an even higher degree of MgO enrichment with respect to the CMC point than melt 10. Therefore, it should shift towards the $MgMoO_4$ + MgO eutectic point faster during the growth process and reach the vicinity of this point in a shorter period of time than melts 4, 7, 9 and 10. In fact, the "mush" appears almost immediately after the start of the growth of crystal 1.

On the other hand, we assume that crystals 2, 3 and 8 (green points in Figure 8) were grown from the melts enriched by MoO_3 with respect to the CMC. Thus, the compositions of their melts should gradually shift towards even larger MoO_3 excess during the growth process. However, such a shift is unlikely to result very quickly in starting the precipitation of MoO_3-enriched secondary phases because the $MgMoO_4$ primary crystallization field is quite far into MoO_3 zone (see Figure 7). This exact situation was observed in reality: neither "mush" formation in the melts nor any secondary phase precipitation in crystals 2, 3 and 8 occurred.

Therefore, the Mg/Mo atomic ratio corresponding to the CMC of $MgMoO_4$ crystal should be slightly lower than the actual composition of crystal 4, i.e., <0.976.

2. The range of retrograde solubility exists in the MgO-enriched boundary of the $MgMoO_4$ homogeneity field (solidus line) and the actual compositions of crystals 5 and 6 (red points in Figure 8) are located in this range. The initial melt compositions of these samples are probably quite strongly enriched in MgO (more so than melt 1) and are already in the vicinity of the $MgMoO_4$ + MgO eutectic at the starting stage of the growth. That is why the "mush" appears just at the start of the growth of these crystals. After some time, the continuous capturing of "mush" by the crystal leads to the removal of some MgO from the melt, a shift of the total melt composition away from the vicinity of the $MgMoO_4$ + MgO eutecti, and, therefore, to the cessation of the formation of new "mush" portions. However, due to the retrograde solubility, the actual compositions of crystals 5 and 6 have lesser MgO concentrations compared to crystal 1 and, even, compared to crystals 4, 7, 9 and 10, despite fact that the melts 5 and 6 had larger concentration of MgO, at least at the first stages of the growth.

3. The MoO_3-enriched boundary of the $MgMoO_4$ homogeneity field probably has also rather complicated shape, as tentatively indicated in Figure 8 (upper panel). That is why the actual compositions of crystals 2 and 3 have very minor differences with the ones for crystals 4 and 7 (see Table 1), whereas the composition of crystal 8 is even slightly MgO-enriched in respect to those of crystals 4 and 7, despite the initial melt compositions for crystals 2, 3 and 8 being (as we assume) MoO_3-enriched in respect to the CMC.

Another possible explanation is that the actual composition of crystal 8 is shifted towards the MoO_3-enriched side, whereas the actual compositions of crystals 4 and 7 are, on the contrary, shifted towards the MgO-enriched side from the corresponding average values given in Table 1 within the limits of the measurement errors (see Figure 8 lower panel). The measurements of the unit cell parameters support this version, as can be seen below. In this case, we can build the supposed MoO_3-enriched boundary of the $MgMoO_4$ homogeneity field with a much simpler and traditional shape, whereas the Mg/Mo atomic ratio corresponding to the CMC should be ~0.977–0.978 in this version.

We have performed an additional XRD analysis to reveal the unit cell parameters of the crystals. For these measurements we ground six pieces taken from different defect-free areas of each sample. TOPAS (Total Pattern Analysis Solutions) software Version 8 was used for the calculations by the Rietveld method. The file with the theoretical structure model of $MgMoO_4$ crystal from the Crystallography Open Database [57] was used as the starting approximation. The revealed unit cell volumes of all the crystals are presented in

Figure 9. The samples on the chart are arranged along the horizontal axis sequentially as their unit cell volume increases.
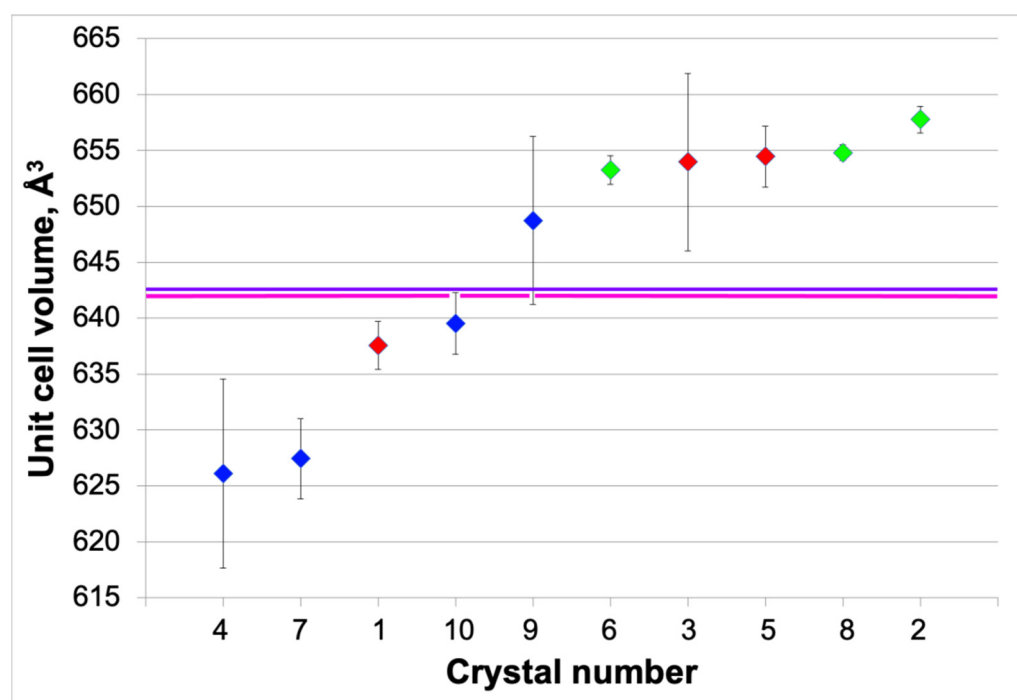

Figure 9. Unit cell volumes of the studied Nd:MgMoO$_4$ crystals. Colours of the experimental points are the same as in Figure 8. Violet and pink lines are the values of MgMoO$_4$ and MgMoO$_4$:0.1 at. % Tm unit cell volumes, according to JCPDS file 21-0961 and [31], respectively.

The values of the unit cell volumes appear to correlate with the "mush" behaviour of the melts during the growth and (to some extent) with the Mg/Mo atomic concentration ratios in the actual measured compositions of the crystals. The largest and rather stable values of the unit cell volume were revealed for crystals 2, 3 and 8, during the growth of which no "mush" appeared at all (green diamonds, Figure 9). Along with that, the actual compositions of crystals 2 and 3 are among the most deficient in MgO, as shown in Table 1. Moreover, according to our assumption (see above), the actual composition of crystal 8 is shifted towards the MoO$_3$-enriched side from the average value given in Table 1 (see Figure 8 lower panel) and in fact, this composition is also among the most MgO-deficient.

As can also be seen from Figure 9, the statistical errors in the unit cell parameters determination are comparatively small for the "mush"-free samples, labeled by green points in Figures 8 and 9. This may be evidence of the high uniformity of chemical compositions of the crystals. It means that the MoO$_3$-enriched boundary of the MgMoO$_4$ crystal homogeneity field lies almost vertically in the MgO-MoO$_3$ phase diagram (Figure 8). Therefore, the crystals grown from MoO$_3$-enriched melts (with respect to the CMC) have nearly the same actual compositions and, correspondingly, very close unit cell parameters, independent of the particular amount of MoO$_3$ excess in the melt.

Samples 5 and 6, red diamonds (during the growth of which the "mush" appeared at the starting stage and then disappeared by itself, see above) can also be tentatively assigned to this group. The actual compositions of these crystals are also among the most MgO-deficient (see Table 1) although, according to our assumptions, their compositions lie at the MgO-enriched boundary of the MgMoO$_4$ homogeneity field (Figure 8). These crystals also have the largest unit cell parameters, comparable with those for crystals 2, 3 and 8. Thus, we can certainly conclude that the largest MgO deficiency in the MgMoO$_4$ crystal composition provides the largest unit cell parameters of the crystal.

However, in contrast to "green" samples 2, 3 and 8, "red" crystals 5 and 6 are characterized by substantial variations in the unit cell volumes at different areas of a sample. We assume that this reflects the fact that beginning parts of these samples were crystallized from quite strongly magnesium-enriched melts. However, then the "mush" was captured by the crystal surface and a significant part of MgO has left the melts. Therefore, the further portions of the crystals were already solidified from the melts with another less MgO-enriched composition, which should lead to changes in the actual crystal compositions. Thus, the actual compositions of different parts of crystals 5 and 6 are slightly different from each other. These differences also reflect a rather strong spread in the unit cell parameters.

Finally, the crystals 4, 7, 9 and 10 (blue diamonds) grown from the initially clear melts with the appearance of "mush" after some period of time, as well as crystal 1 (red diamond), are characterized by essentially lower unit cell parameters than the rest of the samples. Substantial variations in the unit cell volumes are observed for this group. The variations occur both from sample to sample and within different areas of each sample.

According to our assumptions, all these crystals were solidified from the MgO-enriched melts with respect to the CMC, but within a normal (not retrograde) solubility range. The actual compositions of these samples have the least Mg^{2+} deficiency with respect to the stoichiometry, and obviously, they have the least content of magnesium vacations compared to other crystals. Thus, we can conclude that the size of Mg^{2+} ion is smaller than the "size" of Mg vacancy. A similar situation was earlier found for Scheelite-like molybdate crystals [58–60].

Furthermore, we suppose that the solidification of crystals 1, 4, 7, 9 and 10 was accompanied by a comparatively strong shift of the melt compositions and, obviously, of the crystal compositions, like in the case of crystals 5 and 6. Thus, rather strong spreads in the unit cell parameters inside each sample of this group are explainable.

Note that the unit cell volumes of crystals 1 and 10, grown from the same stoichiometric charge completely without any treatment, coincide with each other within the measurement error limits. Moreover, they are very close to the literature data for $MgMoO_4$ (the JCPDS file 21-0961) and for $MgMoO_4$:0.1 at. % Tm crystal [32] (Figure 9, violet and pink lines, correspondingly).

It is clear from the results presented above that the different procedures for the charge preparation (different sequence of the procedures of UHD treatment and calcining) result in different shifts of the starting melt compositions towards different sides from the $MgMoO_4$ CMC. This leads to different "mush" behaviour of the melts and to crystals with slightly different actual compositions and unit cell parameters.

We have also grouped the crystals by the type of components that were treated by UHD and by sequence of the procedures of UHD treatment and calcining (whole charge treatment before calcination 2, 3, 4; whole charge treatment after calcination 5, 6; Nd_2O_3 treatment 7, 8, 9) and then checked for statistically significant differences in unit cell parameters within each a group. Comparisons within the groups were carried out using analysis of variance followed by pairwise comparison of groups using Student's *t*-test with the Kruskal–Wallis correction followed by Dunn's test. The comparison has resulted in the following pairs: samples 2 and 4 (control) differ in parameters *a*, *b* and *V*; sample 7 differs from sample 8 (control) in *a*, *β*, *V* as well as from 9 (control) in *a* and *V*. No other differences were found to be statistically significant between those groupings. These results show that only UHD-treated charges have statistically different unit cell parameters of the grown crystals, which underlines the possible modifying effects of UHDs of charges.

The observed changes may have the same explanation, as suggested by others [16]: after the technical preparation of UHD solution, aggregates of highly diluted initial substances connected to gas nanobubbles may form, which can be retained after repeated dilutions due to the flotation effect [18].

3.2. Actual Nd^{3+} Concentration and Optical Absorption Spectra

Along with the measurements of the actual Mg and Mo concentrations in the samples, the contents of Nd^{3+} and of some accidental impurities in the crystals was also measured. For the majority of the impurities, the measurements were performed by ICP-MS simultaneously with the measurements of Mg and Mo concentrations. For some impurities (e.g., potassium) the refining measurements were also carried out by atomic emission spectroscopy with inductively coupled plasma (ICP-AES) using an of iCAP 6300 duo spectrometer (Thermo Fisher Scientific, Waltham, MA, USA). A set of the multi-element standards (High-Purity Standards, Charleston, SC, USA) was used for calibration.

The measured Nd concentrations are presented in Figure 10. Among the revealed accidental impurities, one should especially mention potassium. Its concentrations are also given in Figure 10.
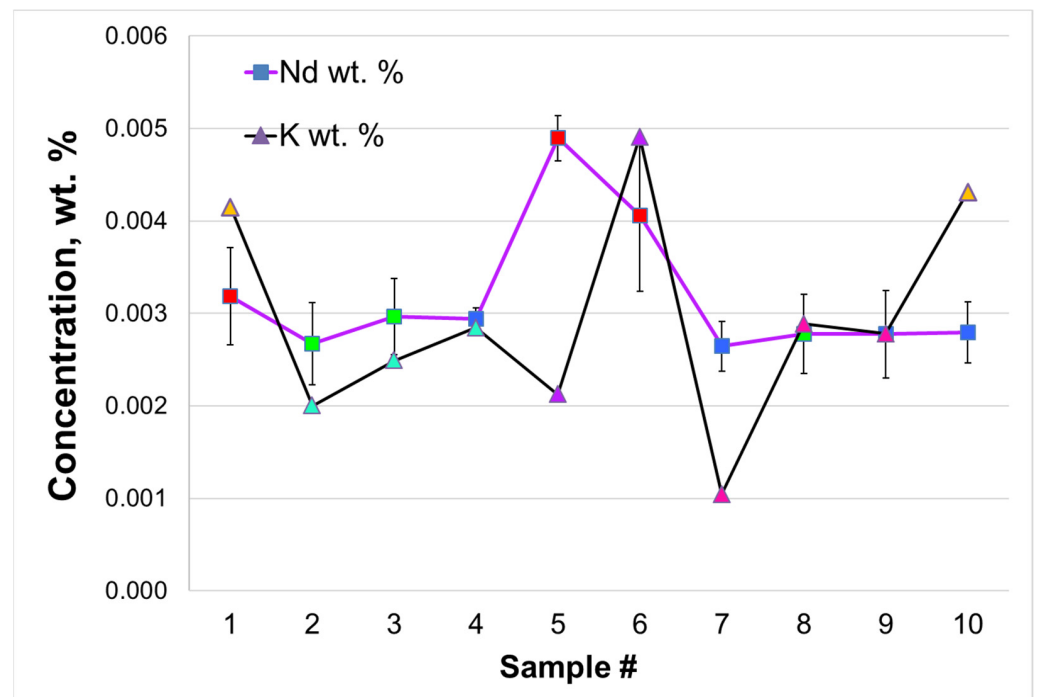

Figure 10. Measured concentrations of Nd^{3+} and K^+ ions in the crystals. Colours of neodymium points are the same as they are for the corresponding samples in Figures 8 and 9; colours of potassium points designate the types of treatment of the charges, and they correspond to the colours of blocks in Figure 3.

The special interest in potassium accidental impurity is due to the fact that the substitution of Mg^{2+} ion for Nd^{3+} is heterovalent in the $MgMoO_4$ lattice and the effective excess positive charge appears in the crystal during such a substitution. It requires a compensation of charge. If no special charge compensator is introduced into the lattice along with Nd^{3+} (as in our case), such compensation occurs in the crystal via the formation of some own non-stoichiometry charged defects—probably magnesium vacancies—according to the following quasi-chemical equation (Kröger-Vink notations):

$$3Mg_{Mg}{}^\times + Nd_2O_3 = 2Nd_{Mg}{}^\bullet + V_{Mg}{}'' + 3MgO \tag{1}$$
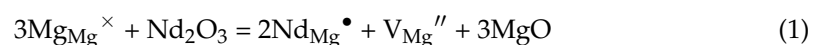
where $Mg_{Mg}{}^\times$ is magnesium ion in its regular site without any effective excess charges, $Nd_{Mg}{}^\bullet$ is neodymium ion in the magnesium site with the effective excess positive charge and $V_{Mg}{}''$ is magnesium vacancy with a double effective excess negative charge.

The formation of additional point defects (like magnesium vacancies) in crystals is an energetically unfavorable process that occurs with difficulty and brings additional internal

energy into a lattice. It partially explains the very low distribution coefficient of Nd^{3+} between $MgMoO_4$ crystal and the melt (see below). However, if a monovalent cation (like K^+) enters into magnesium lattice simultaneously with trivalent neodymium, these two cations compensate the effective excess charges of each other in the frame of the mechanism of conjugate isomorphism, according to the equation:

$$4Mg_{Mg}{}^{\times} + Nd_2O_3 + K_2O = 2Nd_{Mg}{}^{\bullet} + 2K_{Mg}{}' + 4MgO \tag{2}$$
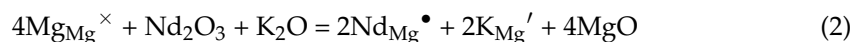
where $K_{Mg}{}'$ is the potassium ion in the magnesium site with the effective excess negative charge.

In this case there is no necessity for the formation of magnesium vacancies, and neodymium entry into the lattice should be facilitated to some extent. That is why it is very important to monitor the existence of such accidental impurities as potassium in the Nd:$MgMoO_4$ crystal.

As can be seen from Equation (2), the mechanism of conjugate isomorphism efficiently works only if the concentrations of the mutually compensating impurities are comparable, which is the case for potassium in our samples (Figure 10). All other revealed accidental impurities that could, in principle, participate in this process with Nd^{3+} in the Nd:$MgMoO_4$ the crystal (other alkali metal ions, or small pentavalent ions that could enter into the Mo^{6+} lattice) appeared to be in too low concentrations in the crystals. Thus, we do not consider these impurities.

An indicator of functioning of the mechanism of conjugate isomorphism between Nd^{3+} and K^+ in the Nd:$MgMoO_4$ crystal should be the correlation between the concentrations of these two ions in the crystals. However, as shown in Figure 10, the correlation is not very strong. At least 3 of 10 samples (5, 7 and 10) apparently do not follow this correlation. It means, at least, that there are some additional factors a having a strong influence on the entry of Nd^{3+} and K^+ into the crystal.

In order to search for these factors, we used different colour pattern to mark experimental points in Figure 10. Marks indicating Nd^{3+} concentrations in the samples (squares) have the same colours as in Figures 8 and 9, i.e., they reflect the "mush" behaviour of melts. Marks indicating potassium concentrations in the samples (triangles) have the same colours as the blocks in Figure 3, i.e., they reflect the type and order of treatment of the charges. It is seen that the Nd^{3+} concentrations rather close to each other, 0.0027–0.0032 wt. % in the majority of the samples (except 5 and 6). This corresponds to the segregation coefficients of 0.0034–0.0041. This is substantially lower than the earlier determined segregation co-efficient of the Tm^{3+} and Cr^{3+} ions in $MgMoO_4$ crystal, which are equal to 0.02 [31] and 0.24 [40], respectively. Neither the type of treatment nor the "mush" behaviour of the melt (its position in respect to the CMC) nor the fluctuations of K^+ concentration from sample to sample had any pronounced effect onto the actual Nd^{3+} content in these samples.

However, samples 5 and 6 contain about 1.5 times larger Nd^{3+} concentrations as compared to the other 8 samples. These samples were grown from the charges that have undergone UHD treatment before calcining (in contrast to all the rest samples) and the growth of these crystals was most likely run from the most MgO-enriched melt, see above. Thus, it is likely that these factors are the main reason for the increased Nd^{3+} content in crystals 5 and 6 and the corresponding segregation coefficients. However, the particular mechanism of such influence is still unclear and requires additional investigation.

The unpolarized optical absorption spectra of all samples in the range of 550–850 nm were measured using a Cary 5000 spectrophotometer (Varian, France) with a measurement step of 0.2 nm at 300 K. The obtained spectra after subtraction of the background of the own host absorption [31] are presented in Figure 11.
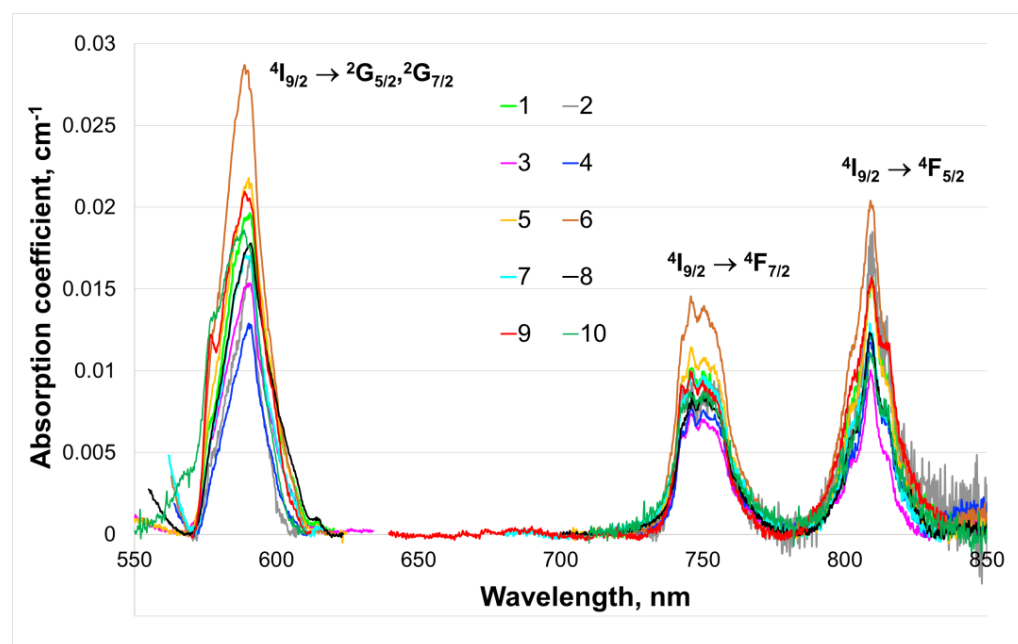
Figure 11. Unpolarized optical absorption spectra of the samples. For the crystals 1–8, the direction of the probe beam is parallel to the *c* crystallographic axis, whereas for the crystals 9–10, it is perpendicular to *c*.

Three characteristic optical absorption bands of Nd^{3+} are seen in the spectra, peaking near 815, 750 and 590 nm. All the bands are very weak due to the very low actual Nd^{3+} concentrations in the samples. The following conclusions can be drawn from the analysis of the observed optical absorption bands:

1. The shapes and peak positions of the bands corresponding to the particular transitions are equal for all the studied samples within the measurement error. The only exception is the additional local peak at ~576.5 nm observed for crystals 9 and 10 but absent for the rest of samples. This difference can be easily explained by different probe beam directions with respect to the crystallographic axes for these two groups of samples (Figure 11 caption).

2. The absorption band with the maximum near 590 nm probably corresponds to the overlapped bands of the $^4I_{9/2} \rightarrow ^2G_{5/2}$ and $^4I_{9/2} \rightarrow ^2G_{7/2}$ transitions of Nd^{3+} ion. According to the theory, for a single kind of Nd^{3+} ion located in a low-symmetry crystal field, the total number of Stark components should be equal to seven for these two transitions (in sum). However, except for the above-noted additional local peak at 576.5 nm in samples 9 and 10, no local Stark components are distinguishable at 300 K. Obviously, this is the result of too large a number of strongly overlapped elementary lines being located within a rather narrow spectral range.

3. The absorption band near 750 nm should be attributed to the $^4I_{9/2} \rightarrow ^4F_{7/2}$ transition of Nd^{3+} ion. Four local maxima at the wavelengths of ~742,5~745,2~750 and ~755 nm can be clearly distinguished for all samples in this spectral range. Obviously, these maxima correspond to the transitions between the lowest Stark component of the $^4I_{9/2}$ ground state and all four Stark components of the $^4F_{7/2}$ excited state. According to the theory, just this number of Stark components should exist for this transition in the case of a single kind of Nd^{3+} ion located in a low-symmetry crystal field.

4. The absorption band near 800 nm belongs to the $^4I_{9/2} \rightarrow ^4F_{5/2}$ transition of neodymium. Similarly, three local maxima at the wavelengths of ~802, ~809,2 and ~815 nm can be distinguished for all samples. These maxima correspond to the transitions between the lowest Stark component of the $^4I_{9/2}$ ground state and all three Stark components of the $^4F_{5/2}$ excited state. Again, according to the theory, just this number of the Stark components

should be observed for the $^4I_{9/2} \rightarrow ^4F_{5/2}$ transition in the case of a single kind of Nd^{3+} ion located in a low-symmetry crystal field.

Therefore, within the experimental error, only one kind of Nd^{3+} optical center was revealed in $Nd:MgMoO_4$, regardless of the peculiarities of the sample growth or treatment of the charges. These centers are probably located in the low-symmetry crystal field of the Mg1 $4g$ site. No additional Nd^{3+} centers (located in either the Mg2 $4i$ site or in any disturbed site, for example, associates of Nd^{3+} ions with charge compensating point defects) were revealed by optical absorption spectroscopy analysis at 300 K. Further attempts to search for these centers should be conducted with the help of more sensitive methods such as optical absorption spectroscopy at 4.2 K or EPR spectroscopy.

On the other hand, the absorption intensities vary from sample to sample. We believe these variations are caused by differences in the actual Nd^{3+} concentrations in the crystals. According to the Lambert–Booger–Behr law, the peak optical absorption cross-section was calculated for this transition for each $Nd:MgMoO_4$ crystal. The average value appeared to be $1.9 \pm 0.3 \times 10^{-20}$ cm^2. It is less than for monoclinic molybdate $Nd^{3+}:KY(MoO_4)_2$ ($E\|Nm$ (3.8×10^{-20} cm^2), $E\|Ng$ (7×10^{-20} cm^2) and $E\|Np$ (4×10^{-20} cm^2) [58] or for tetragonal Scheelite-like tungstate $Nd^{3+}:PbWO_4$ (2.75×10^{-20} cm^2 and 4.75×10^{-20} cm^2 for σ-($E \perp c$) and π-($E\|c$) polarizations, respectively [59].

Note that quite close values of Nd^{3+} optical absorption coefficients for samples 1–4 and 7–10 reproduce/confirm rather small variations in the actual neodymium concentrations in the crystals revealed by ICP MS analysis. Meanwhile, the increased Nd^{3+} optical absorption coefficients for samples 5 and 6 reflect the increased actual neodymium concentrations in the latter samples although, unfortunately, with substantial measurement errors.

3.3. Nd^{3+} Luminescence Properties

We measured the polarized stationary luminescence spectra and the luminescence decay kinetics for all samples at T = 300 K. The luminescence spectra were measured in the spectral range of 860–1160 nm with a step of 0.5 nm in the ranges of luminescence bands 870–950 nm and 1050–1100 nm, and 2 nm in other ranges where the luminescence is absent. The excitation was performed into the Nd^{3+} absorption band of the $^4I_{9/2} \rightarrow ^4F_{5/2}$ transition by an AlGaAs diode laser (Laserland, Wuhan, China) emitting at 808 nm. The laser beam spot was falling perpendicularly at the center of a flat sample facet. The size of the facet considerably exceeded the spot size. The measurements were performed at L-configuration. A Glan prism was used for the polarization of the luminescence emission. The exciting diode laser emits strongly polarized radiation. The polarization planes of the diode radiation and of the Glan prism were perpendicular to each other in order to minimize the influence of the exciting emission reflected from the sample on the shape of the luminescence spectra. The luminescence emission was dispersed by an MDR-1 monochromator (LOMO, St. Petersburg, Russia) and then detected by a FEU-83 photomultiplier tube or by an InSb photodiode.

The measurements of the luminescence decay kinetics were performed using the same experimental setup, with the following peculiarities: (1) the exciting laser diode was operated in the regime of short pulses (not in the CW-regime, as for the stationary luminescence spectra); (2) Glan prism was absent; (3) electric signal from the photomultiplier tube or from the InSb photodiode was registered and digitized by a TBS 1202B digital oscilloscope (Tektronix, Beaverton, OR, USA).

Two characteristic Nd^{3+} luminescence bands were observed in both of the above-specified ranges. They correspond to the $^4F_{3/2} \rightarrow ^4I_{9/2}$ and $^4F_{3/2} \rightarrow ^4I_{11/2}$ spectral transitions. An example of the polarized luminescence spectra of $Nd:MgMoO_4$ crystals is presented in Figure 12. It consists of two bands corresponding to the $^4F_{3/2} \rightarrow ^4I_{9/2}$ and $^4F_{3/2} \rightarrow ^4I_{11/2}$ transitions of the Nd^{3+} ion. The intensity ratio of these two luminescence bands depends on the polarization. Stark structures of the bands are practically unresolved at 300 K, although non-Gaussian shapes of the bands are evident.
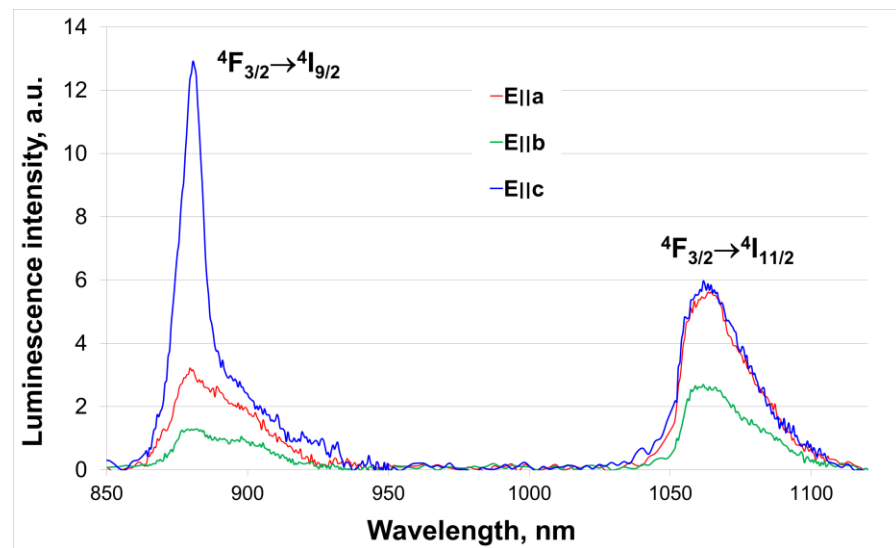
Figure 12. Example of the polarized luminescence spectra of the Nd:MgMoO$_4$ crystal (λ_{ex} = 808 nm, T = 300 K).

Figure 13 presents the relative intensities of the luminescence peak at 881 nm (E‖c polarization) for all the studied samples along with the optical absorption coefficients of the same samples at 745.6 nm. The arbitrary units of the luminescence intensities are scaled for the convenience of comparison with the absorption intensities.
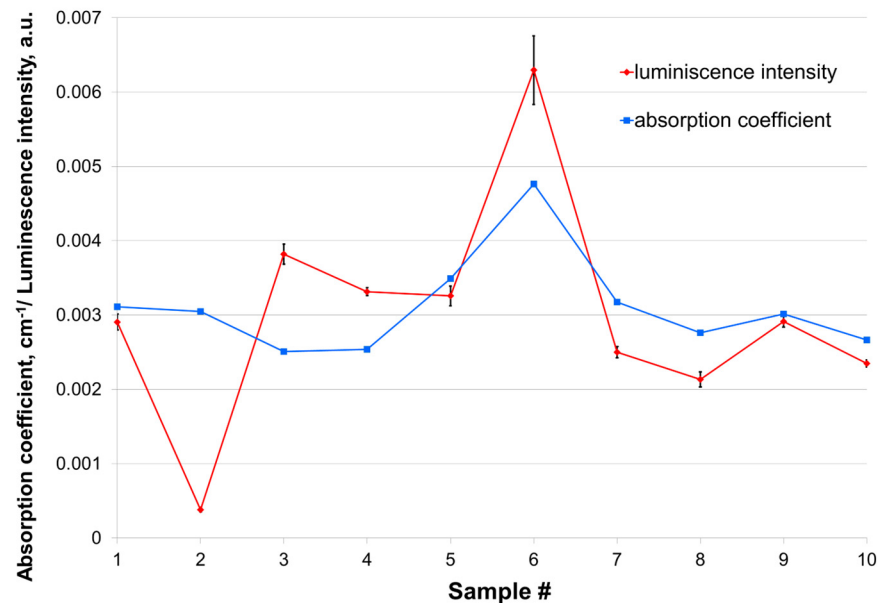

Figure 13. Luminescence intensities at λ = 881 nm (E‖c polarization) and optical absorption coefficients of the samples at λ = 745.6 nm. T = 300 K.

A rather good correlation is observed between the relative absorption and luminescence intensities from sample to sample. In particular, the increased value of the absorption for sample 6 corresponds to a similarly increased value of the luminescence intensity for the same sample. This can be easily explained by the increased Nd^{3+} concentration in this sample (Figure 10).

The only evident exception is sample 2. It has an actual Nd^{3+} concentration comparable with that for all other crystals except 5 and 6 and an absorption intensity comparable with that for all other crystals except 6 (Figure 10). However, the luminescence of this crystal

is strongly (by an order of magnitude) reduced as compared to the other crystals. The reasons for this can be either the reduced probability of the spectral transition or the luminescence quenching.

For verification of the first hypothesis, we measured the luminescence decay kinetics for all crystals. The luminescence was monitored at a wavelength of 880 nm. The typical view of the measured kinetics is presented in Figure 14.
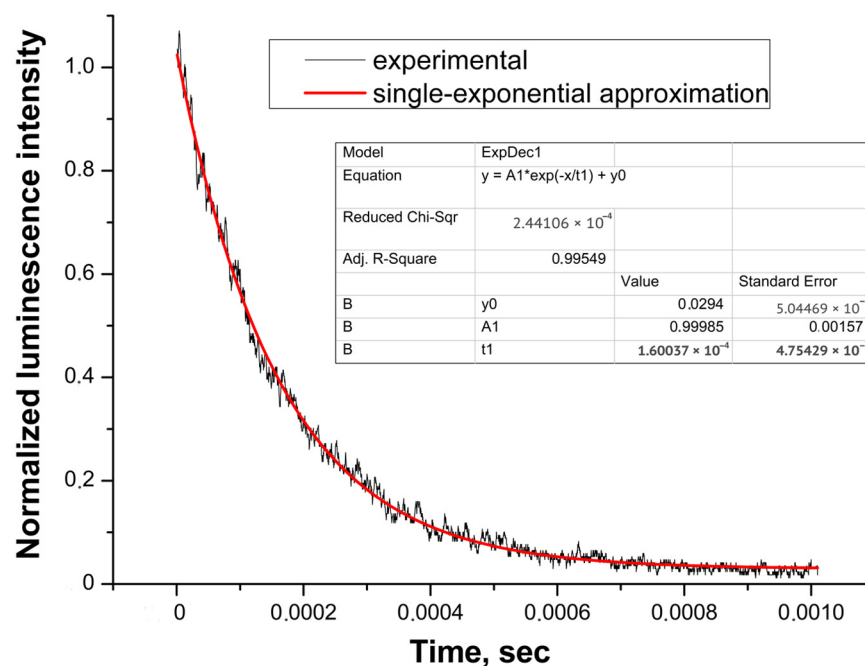

Figure 14. Luminescence decay kinetics of the studied Nd:MgMoO$_4$ crystals (λ_{ex} = 808 nm, λ_{mon} = 880 nm, T = 300 K).

The decay kinetics are well approximated by the single-exponential law for all the studied crystals, indicating the presence of a single kind of luminescent center and the absence of any non-radiative excited energy transfer. The relationship between the decay times and the luminescence intensities of the samples is presented in Figure 15.

As seen in Figure 15, the values of the luminescence lifetimes are 150–170 μs—the most out of all the samples. These values are typical for the $^4F_{3/2}$ excited state of Nd^{3+} ions. Sample 6 (red point in Figure 15) is the specific case among the studied samples: its higher luminescence intensity is caused by an increased Nd^{3+} concentration (see above, Figure 13). Blue points, corresponding to all remaining samples, are rather close to a reciprocal dependence (red line) between the luminescence intensity and the lifetime (the higher probability of the transition, the brighter the luminescence, and the faster the depopulation of the excited state) including sample 2, which demonstrates the weakest luminescence and the longest lifetime. However, a slight increase in the lifetime (by approximately 15%) certainly cannot explain a very strong (by an order of magnitude) reduction of the luminescence intensity. There is definitely an additional mechanism responsible for this reduction. Additional studies are required to elaborate this mechanism.

Note that charge 2 has undergone type 1 treatment, which included UHD treatment of the main charge components (not only Nd$_2$O$_3$ dopant, as in the case of charge 7) in contrast to the charges 1, 3, 4, 6 and 8–10, which have undergone only control treatments or have on undergone treatments at all (see Section 2.2 and Figure 3). Such an UHD treatment is, presumably, the most suitable for modifying effects on charges compared to all other charges. The reduction of the luminescence intensity in sample 2 could be related to UHD treatment of the charge.
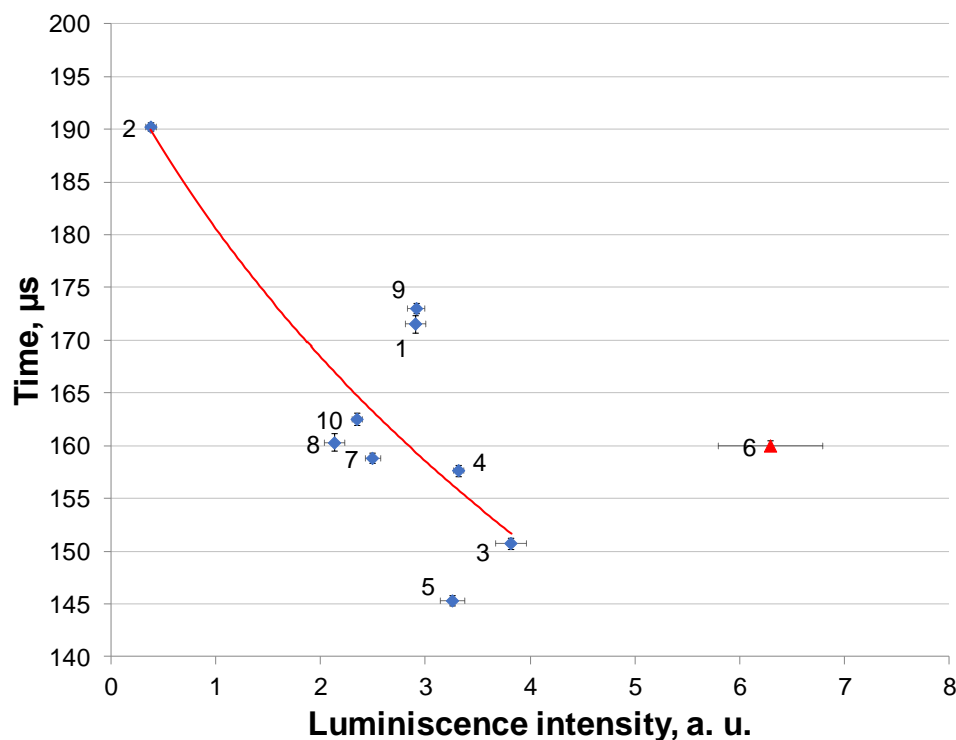
Figure 15. Luminescence decay times versus luminescence intensities of the studied Nd:MgMoO$_4$ samples. Explanations of the colors are given in the main text.

4. Conclusions and Prospects

The influence of the initial charge treatment by ultrahigh dilution technology on the growth of single crystals from these charges and on the properties of the obtained crystals was investigated for MgMoO$_4$ crystals doped by 1 at. % of Nd^{3+}. It was revealed that:

1. The congruently melting composition of Nd:MgMoO$_4$ is in the range of a slight MoO$_3$ excess (MgO deficiency) with respect to MgO:MoO$_3$ = 1:1 stoichiometry. The wetting of MgO + MoO$_3$ chemicals with a water-ethanol solution followed by drying and calcining (solid-phase synthesis) probably leads to some shift of the MgO:MoO$_3$ ratio towards MoO$_3$ excess. On the contrary, wetting of the pre-sintered Nd:MgMoO$_4$ charge by a similar solution followed by drying probably leads to some shift of the MgO:MoO$_3$ ratio towards MgO excess that results in precipitation of MgO-enriched secondary phases in the melts during both the Czochralski crystal growth and the pre-melting of the charges.

2. Nd:MgMoO$_4$ crystals grown from slightly MoO$_3$-enriched melts have quite stable chemical compositions with a MgO/MoO$_3$ molar ratio of 0.974–0.977 and stable unit cell parameters (a = 10.34–10.35 Å; b = 9.34–9.37 Å; c = 7.062–7.072 Å; $β$ = 106.88–106.96°; V = 653.25–657.74 Å^3). The crystals grown from the most highly MgO-enriched melts have nearly the same compositions and unit cell parameters due to the area of retrograde solubility, which probably exists in the MgO-MoO$_3$ system. The crystals grown from the modestly MgO-enriched melts have more MgO-enriched compositions and reduced (and quite unstable) unit cell parameters. UHD-treatment has only a small yet statistically significant influence on unit cell parameters within the similarly treated groups. These conclusions should be verified by the further investigations of the system, which will be performed at the next stage of the research.

3. The distribution coefficient of Nd^{3+} between Nd:MgMoO$_4$ crystal and melt was ~0.004 for most of the studied samples. However, wetting of the pre-sintered Nd:MgMoO$_4$ charge by a water-alcohol solution followed by drying (probably leading to some shift of the MgO:MoO$_3$ ratio in the Nd:MgMoO$_4$ melt towards MgO excess) resulted in an increase of the Nd^{3+} distribution coefficient by 1.5 times. Some influence of potassium accidental impurity on the Nd^{3+} distribution coefficient should not be excluded as well.

4. According to the 300 K optical absorption spectrum and the luminescence decay kinetics of the studied crystals, Nd^{3+} forms only one kind of optical center located in a single low-symmetry crystallographic position on the $MgMoO_4$ lattice. The search for additional optical centers will be continued at the next stage of the research by use of low-temperature optical and EPR-spectroscopy. The peak absorption cross-section at the wavelength of 745.6 nm ($^4I_{9/2} \rightarrow {}^4F_{7/2}$ transition) is $(1.9 \pm 0.3) \times 10^{-20}$ cm^2. The luminescence lifetime at 300 K varies in the range of 145–190 nm and probably depends on the particular crystal composition (MgO/MoO_3 molar ratio).

5. The crystal grown from the charge, which underwent treatment by ultrahigh dilution technology before its solid-phase synthesis, has strongly reduced Nd^{3+} luminescence, as compared to all the rest studied $Nd:MgMoO_4$ crystals. The reason for such a reduction is most likely related to the charge treatment by UHD. There may be some additional effects of UHD treatment, but they are strongly blurred by the influence of the water-ethanol solution itself on the charge and on the melt composition (see conclusion 1). Thus, we will use an alternative way of UHD treatment at the next stage of the research that is not connected with use of water-ethanol solution.

Author Contributions: Conceptualization, K.A.S.; methodology, K.A.S. and A.I.T.; software, D.A.L. and O.N.L.; validation, K.V.K., Y.I.Z. and S.K.P.; formal analysis, Y.I.Z., P.A.V., V.V.V. and E.V.C.; investigation, Y.S.D., P.A.V., K.I.R., V.V.V. and E.V.C.; resources, D.A.L., A.I.T., S.K.P. and K.I.R.; data curation, Y.S.D.; writing—original draft preparation, K.A.S.; writing—review and editing, Y.S.D.; visualization, K.V.K.; supervision, O.N.L.; project administration, K.A.S. All authors have read and agreed to the published version of the manuscript.

Data Availability Statement: Data is contained within the article.

Conflicts of Interest: The authors declare that this study received funding from OOO "NPF "MATERIA MEDICA HOLDING". The funder had the following involvement with the study: sponsored the study, took part in the design of the experiments and the manuscript writing. The authors have disclosed those interests fully to the "Crystals" Journal.

References

1. Gudkov, S.V.; Penkov, N.V.; Baimer, I.V.; Lyakhov, G.A.; Pustovoy, V.I.; Simakin, A.V.; Sarimov, R.M.; Scherbakov, I.A. Effect of Mechanical Shaking on the Physicochemical Properties of Aqueous Solutions. *Int. J. Mol. Sci.* **2020**, *21*, 8033. [CrossRef] [PubMed]
2. Gudkov, S.V.; Baimler, I.V.; Uvarov, O.V.; Smirnova, V.V.; Volkov, M.Y.; Semenova, A.A.; Lisitsyn, A.B. Influence of the Concentration of Fe and Cu Nanoparticles on the dynamics of the Size Distribution of Nanoparticles. *Front. Phys.* **2020**, *8*, 622551. [CrossRef]
3. Ryzhkina, I.S.; Murtazina, L.I.; Kiseleva, Y.V.; Konovalov, A.I. Self-organization and physicochemical properties of aqueous solutions of the antibodies to interferon gamma at ultrahigh dilution. *Dokl. Phys. Chem.* **2015**, *462*, 110–114. [CrossRef]
4. Tarasov, S.A.; Gorbunov, E.A.; Don, E.S.; Emelyanova, A.G.; Kovalchuk, A.L.; Yanamala, N.; Schleker, A.S.S.; Klein-Seetharaman, J.; Groenestein, R.; Tafani, J.-P.; et al. Insights into the Mechanism of Action of Highly Diluted Biologics. *J. Immunol.* **2020**, *205*, 1345–1354. [CrossRef]
5. Lobyshev, V.I. Evolution of High-Frequency Conductivity of Pure Water Samples Subjected to Mechanical Action: Effect of a Hypomagnetic Filed. *Phys. Wave Phenom.* **2021**, *29*, 98–101. [CrossRef]
6. Penkov, N.V. Temporal dynamics of scattering properties of deionized water. *Phys. Wave Phenom.* **2020**, *28*, 135–139. [CrossRef]
7. Slatinskaya, O.V.; Pyrkov, Y.N.; Filatova, S.A.; Guryev, D.A.; Penkov, N.V. Study of the Effect of Europium Acetate on the Intermolecular Properties of Water. *Front. Phys.* **2021**, *9*, 641110. [CrossRef]
8. Lobyshev, V.I. Biological Activity of Solutions of Substances at Low and Ultra Low Concentrations. *Biophysics* **2022**, *67*, 523–533. [CrossRef]
9. Malarczyk, E.; Pazdzioch-Czochra, M.; Grąz, M.; Kochmańska-Rdest, J.; Jarosz-Wilkołazka, A. Nonlinear changes in the activity of the oxygen-dependent demethylase system in Rhodococcus erythro-polis cells in the presence of low and very low doses of formaldehyde. *Nonlinear Biomed. Phys.* **2011**, *5*, 9. [CrossRef]

10. Floris, I.; Appel, K.; Rose, T.; Lejeune, B. 2LARTH®, a micro-immunotherapy medicine, exerts anti-inflammatory effects in vitro and reduces TNF-α and IL-1β secretion. *J. Inflamm. Res.* **2018**, *11*, 397–405. [CrossRef]

11. Floris, I.; Rose, T.; Rojas, J.A.C.; Appel, K.; Roesch, C.; Lejeune, B. Pro-Inflammatory Cytokines at Ultra-Low Dose Exert Anti-Inflammatory Effect In Vitro: A Possible Mode of Action Involving Sub-Micron Particles? *Dose-Response* **2020**, *18*, 1–11. [CrossRef]

12. Jacques, C.; Floris, I.; Lejeune, B. Ultra-Low Dose Cytokines in Rheumatoid Arthritis, Three Birds with One Stone as the Rationale of the 2LARTH®Micro-Immunotherapy Treatment. *Int. J. Mol. Sci.* **2021**, *22*, 6717. [CrossRef]

13. Kim, W.-K.; Kim, Y.H.; Hong, G.; Kim, J.M.; Han, J.G.; Lee, J.Y. Effect of Hydrogen Nanobubbles on the Mechanical Strength and Watertightness of Cement Mixtures. *Materials* **2021**, *14*, 1823. [CrossRef]

14. Kamentsev, K.E.; Bush, A.A. The superconducting properties of YBa$_2$Cu$_3$O$_y$ ceramics fabricated using ultrahigh dilution technology. *Ceram. Int.* **2022**, *48*, 32196–32204. [CrossRef]

15. Spitsin, A.I.; Bush, A.A.; Kamentsev, K.E. Piezoelectric and dielectric properties of Bi$_3$TiNbO$_9$ prepared by hot pressing from powders activated using the serial dilution method. *Sci. Rep.* **2020**, *10*, 22198. [CrossRef] [PubMed]

16. Lyakhov, G.A.; Shcherbakov, I.A. Approaches to the Physical Mechanisms and Theories of Low-Concentration Effects in Aqueous Solutions. *Phys. Wave Phen.* **2019**, *27*, 79–86. [CrossRef]

17. Bunkin, N.F.; Shkirin, A.V.; Ninham, B.W.; Chirikov, S.N.; Chaikov, L.L.; Penkov, N.V.; Kozlov, V.A.; Gudkov, S.V. Shaking-induced aggregation and flotation in immunoglobulin dispersions: Differences between water and water-ethanol mixtures. *ACS Omega* **2020**, *5*, 14689–14701. [CrossRef]

18. Agarwal, A.; Ng, W.J.; Liu, Y. Principle and applications of microbubble and nanobubble technology for water treatment. *Chemosphere* **2011**, *84*, 1175–1180. [CrossRef]

19. Chikramane, P.S.; Kalita, D.; Suresh, A.K.; Kane, S.G.; Jayesh, R.B. Why Extreme Dilutions Reach Non-zero Asymptotes: A Nanoparticulate Hypothesis Based on Froth Flotation. *Langmuir* **2012**, *28*, 15864–15875. [CrossRef]

20. Grzegorczyk-Frańczak, M.; Barnat-Hunek, D.; Materak, K.; Łagód, G. Influence of Water with Oxygen and Ozone Micro-Nano Bubbles on Concrete Physical Properties. *Materials* **2022**, *15*, 7938. [CrossRef]

21. Kim, W.-K.; Hong, G.; Kim, Y.-H.; Kim, J.-M.; Kim, J.; Han, J.-G.; Lee, J.-Y. Mechanical Strength and Hydration Characteristics of Cement Mixture with Highly Concentrated Hydrogen Nanobubble Water. *Materials* **2021**, *14*, 2735. [CrossRef]

22. Shen, W.; Mukherjee, D.; Koirala, N.; Hu, G.; Lee, K.; Zhao, M.; Li, J. Microbubble and nanobubble-based gas flotation for oily wastewater treatment: A review. *Environ. Rev.* **2022**, *30*, 359–379. [CrossRef]

23. Ulatowski, K.; Sidorski, M.; Sobieszuk, P. Oil-contaminated Surface Cleaning using Oxygen and Nitrogen Nanobubbles. *J. Phys. Conf. Ser.* **2020**, *1681*, 012017. [CrossRef]

24. Lesin, V.I.; Koksharov, Y.A.; Khomutov, G.B. Magnetic nanoparticles in petroleum. *Pet. Chem.* **2010**, *50*, 102–105. [CrossRef]

25. Uitert, L.G.; Rubin, J.J.; Bonner, W.A. Preparation of Single Crystals of Tungstates and Molybdates of a Number of Divalent Metal Ions. *J. Am. Ceram. Soc.* **1963**, *46*, 512. [CrossRef]

26. Litovskina, L.P.; Meil'man, M.L.; Andrianov, V.G.; Sergeeva, N.I. Electron paramagnetic resonance of Cr^{3+} ions in MgMoO$_4$ monocrystals. *J. Struct. Chem.* **1966**, *6*, 615–616. [CrossRef]

27. Spasskii, D.A.; Kolobanov, V.N.; Mikhaïlin, V.V.; Berezovskaya, L.Y.; Ivleva, L.I.; Voronina, I.S. Luminescence peculiarities and optical properties of MgMoO$_4$ and MgMoO$_4$:Yb crystals. *Opt. Spectrosc.* **2009**, *106*, 556–563. [CrossRef]

28. Mikhailik, V.; Kraus, H.; Wahl, D.; Mykhaylyk, M.S. Studies of electronic excitations in MgMoO$_4$, CaMoO$_4$ and CdMoO$_4$ crystals using VUV synchrotron radiation. *Phys. Status Solidi B* **2005**, *242*, 17–19. [CrossRef]

29. Mikhailik, V.B.; Kraus, H.; Itoh, M.; Iri, D.; Uchida, M. Radiative decay of self-trapped excitons in CaMoO$_4$ and MgMoO$_4$ crystals. *J. Phys. Condens. Matter* **2005**, *17*, 7209–7218. [CrossRef]

30. Litovskina, L.P. Electron paramagnetic resonance of ions of the 3d and 4f groups in single crystals of MgMoO$_4$. *J. Struct. Chem.* **1967**, *7*, 575–577. [CrossRef]

31. Subbotin, K.; Titov, A.; Lis, D.; Zimina, Y.; Didenko, Y.; Elabedine, G.Z.; Eremeev, K.; Solé, R.M.; Aguiló, M.; Volkov, P.; et al. Growth, structure refinement, thermal expansion and optical spectroscopy of Tm^{3+}-doped MgMoO$_4$. *Opt. Mater.* **2023**, *138*, 113648. [CrossRef]

32. Zhukovskii, V.M.; Tkachenko, E.V.; Rakova, T.A. Russ. Phase relations in the MoO3-MgMoO4 system. *J. Inorg. Chem.* **1970**, *15*, 3326–3328. (In Russian)

33. Kaminskii, A.A. *Laser Crystals*; Springer: Berlin/Heidelberg, Germany, 1981.

34. Mikhailik, V.B.; Kraus, H.; Kapustyanyk, V.; Panasyuk, M.; Yu, P.; Tsybulskyi, V.; Vasylechko, L. Structure, luminescence and scintillation properties of the MgWO$_4$—MgMoO$_4$ system. *J. Phys. Condens. Matter* **2008**, *20*, 365219. [CrossRef]

35. Santiago, A.A.G.; Oliveira, M.C.; Ribeiro, R.A.P.; Tranquilin, R.L.; Longo, E.; de Lázaro, S.R.; Motta, F.V.; Bomio, M.R.D. Atomistic Perspective on the Intrinsic White-Light Photoluminescence of Rare-Earth Free MgMoO$_4$ Nanoparticles. *Cryst. Growth Des.* **2020**, *20*, 6592–6603. [CrossRef]

36. Gancheva, M.; Rojac, T.; Iordanova, R.; Piroeva, I.; Ivanov, P. Structural and optical properties of MgMoO$_4$ prepared by mechanochemical technique. *Ceram. Int.* **2022**, *48*, 17149–17156. [CrossRef]

37. Xavier, C.S.; de Moura, A.P.; Longo, E.; Varela, J.A.; Zaghete, M.A. Synthesis and Optical Property of MgMoO$_4$ Crystals. *Adv. Mater. Res.* **2014**, *975*, 243–247. [CrossRef]

38. Zhang, L.; He, W.; Shen, K.; Liu, Y.; Guo, S. Controllable synthesis of hierarchical MgMoO$_4$ nanosheet-arrays and nano-flowers assembled with mesoporous ultrathin nanosheets. *J. Phys. Chem. Solids* **2018**, *115*, 215–220.

39. Amberg, M.; Günter, J.R.; Schmalle, H.; Blasse, G. Preparation, crystal structure, and luminescence of magnesium molybdate and tungstate monohydrates, MgMoO$_4$·H$_2$O and MgWO$_4$·H$_2$O. *J. Solid State Chem.* **1988**, *77*, 162–169. [CrossRef]

40. Li, L.; Huang, Y.; Zhang, L.; Lin, Z.; Wang, G. Growth, Mechanical, Thermal and Spectral Properties of Cr^{3+}:MgMoO$_4$ Crystal. *PLoS ONE* **2012**, *7*, e30327. [CrossRef]

41. Morishita, M.; Kinoshita, Y.; Nozaki, A.; Yamamoto, H. Thermodynamic properties for MMoO$_4$ (M = Mg, Sr and Ba) as the end-members of the yellow phases formed in the nuclear fuel waste glasses. *Appl. Geochem.* **2018**, *98*, 310–320. [CrossRef]

42. Koç, H.; Köse, O.; Eser, E. Low-temperature heat capacities for EMoO$_4$ (E = Mg, Sr, Ba) substances formed in nuclear fuel waste glasses. *Prog. Nucl. Energy* **2022**, *143*, 104054. [CrossRef]

43. Han, G.; Xiao-Bin, Z.; Wen-Ting, C.; Zhi-Feng, Y.; Jian-Fu, P.; Ling-Yun, L.; Yan, Y. Optical Spectroscopic Properties of Yb^{3+}-doped MgMoO$_4$ Crystal Grown by the TSSG Method. *Chin. J. Struct. Chem.* **2017**, *36*, 631–639. [CrossRef]

44. Cavalli, E.; Belletti, A.; Brik, M.G. Optical spectra and energy levels of the Cr^{3+} ions in MWO$_4$ (M = Mg, Zn, Cd) and MgMoO$_4$ crystals. *J. Phys. Chem. Solids* **2008**, *69*, 29–34. [CrossRef]

45. Du, P.; Yu, J.S. Photoluminescence and cathodoluminescence properties of Eu^{3+} ions activated AMoO$_4$ (A = Mg, Ca, Sr, Ba) phosphors. *Mater. Res. Bull.* **2015**, *70*, 553–558. [CrossRef]

46. Zhou, L.-Y.; Wei, J.-S.; Yi, L.-H.; Gong, F.-Z.; Huang, J.-L.; Wang, W. A promising red phosphor MgMoO$_4$:Eu^{3+} for white light emitting diodes. *Mater. Res. Bull.* **2009**, *44*, 1411–1414. [CrossRef]

47. Kim, J.D.; Cho, S. Optical Properties of MgMoO$_4$: Dy^{3+}, Eu^{3+} Phosphors Prepared with Different Eu^{3+} Molar Ratios. *J. Korean Inst. Electr. Electron. Mater. Eng.* **2016**, *29*, 186–191.

48. Ran, W.; Wang, L.; Yang, M.; Kong, X.; Qu, D.; Shi, J. Enhanced energy transfer from Bi^{3+} to Eu^{3+} ions relying on the criss-cross cluster structure in MgMoO$_4$ phosphor. *J. Lumin.* **2017**, *192*, 141–147. [CrossRef]

49. Loiko, P.; Serres, J.M.; Mateos, X.; Aguiló, M.; Díaz, F.; Zhang, L.Z.; Lin, Z.B.; Lin, H.F.; Zhang, G.; Yumashev, K.; et al. Monoclinic Tm^{3+}:MgWO$_4$: Novel crystal for continuous-wave and passively Q-switched lasers at ~2 μm. *Opt. Lett.* **2017**, *42*, 1177–1180. [CrossRef]

50. Miller, J.E.; Jackson, N.B.; Evans, L.; Sault, A.G.; Gonzales, M.M. The Formation of Active Species for Oxidative Dehydrogenation of Propane on Magnesium Molybdates. *Catal. Lett.* **1999**, *58*, 147–152.

51. Cadus, L.E.; Abello, M.C.; Gomez, M.F.; Rivarola, J.B. Oxidative Dehydrogenation of Propane over Mg−Mo−O Catalysts. *Ind. Eng. Chem. Res.* **1996**, *35*, 14–18.

52. Bakakin, V.; Klevtsova, R.; Gaponenko, L. Crystal structure of magnesium molybdate MgMoO$_4$ an example of modified closest packing with two types of tetrahedral. *Kristallografiya* **1982**, *27*, 38–42.

53. Wilbur, S.M.; Sugiyama, N.; McCurdy, E. Optimizing Performance for a Collision/Reaction Cell ICP-MS System Operating in Helium Collision Mode. *Spectrosc. Appl. ICPICP-MS Suppl.* **2010**, *25*, 11.

54. Epshtein, O.I. Modifier and Method for Changing the Electrophysical and Magnetic Properties of Ceramics. Application Filed by Limited Liability Company Scientific and Production Firm "Materia Medica Holding". Patent RU 2768221 C1, 23 March 2022.

55. Crystallography Open Database. Available online: http://www.crystallography.net/cod/9009632.html (accessed on 1 October 2021).

56. Haynes, W.M. *CRC Handbook of Chemistry and Physics*, 92nd ed.; CRC Press: Boca Raton, FL, USA, 2011; p. 474. ISBN 1-4398-5511-0.

57. Chen, C.W. and Hensley, S. Amplitude-based height-reconstruction techniques for synthetic aperture ladar systems. *JOSA A* **2005**, *22*, 529–538. [CrossRef] [PubMed]

58. Dudnikova, V.B.; Antonov, D.I.; Zharikov, E.V.; Eremin, N.N. Cation-Deficient Sodium–Gadolinium Molybdates of Variable Composition. Simulation of the Properties and Local Structure. *Crystallogr. Rep.* **2023**, *68*, 537–545. [CrossRef]

59. Dudnikova, V.B.; Zharikov, E.V. Atomistic simulation of sodium–gadolinium molybdate of stoichiometric (Na$_{1/2}$Gd$_{1/2}$MoO$_4$) and cation-deficient (Na$_{2/7}$Gd$_{4/7}$MoO$_4$) compositions. *Phys. Solid State* **2017**, *59*, 866–877. [CrossRef]

60. Kuz'micheva, G.M.; Kaurova, I.A.; Rybakov, V.B.; Eistrikh- Geller, P.A.; Zharikov, E.V.; Lis, D.A.; Subbotin, K.A. Influence of initial charge composition and growth/annealing atmospheres on the structural parameters of Czochralski-grown (NaxGd1-x)MoO4 crystals. *Cryst. Eng. Commun.* **2016**, *18*, 2921. [CrossRef]